

REPORT DOCUMENTATION PAGE			Form Approved OMB NO. 0704-0188		
<p>The public reporting burden for this collection of information is estimated to average 1 hour per response, including the time for reviewing instructions, searching existing data sources, gathering and maintaining the data needed, and completing and reviewing the collection of information. Send comments regarding this burden estimate or any other aspect of this collection of information, including suggestions for reducing this burden, to Washington Headquarters Services, Directorate for Information Operations and Reports, 1215 Jefferson Davis Highway, Suite 1204, Arlington VA, 22202-4302. Respondents should be aware that notwithstanding any other provision of law, no person shall be subject to any penalty for failing to comply with a collection of information if it does not display a currently valid OMB control number.</p> <p>PLEASE DO NOT RETURN YOUR FORM TO THE ABOVE ADDRESS.</p>					
1. REPORT DATE (DD-MM-YYYY) 23-11-2015		2. REPORT TYPE Final Report		3. DATES COVERED (From - To) 23-Aug-2010 - 22-Aug-2015	
4. TITLE AND SUBTITLE Final Report: Analysis of Electrical Transport and Noise Mechanisms in Amorphous Silicon			5a. CONTRACT NUMBER W911NF-10-1-0410		
			5b. GRANT NUMBER		
			5c. PROGRAM ELEMENT NUMBER 611102		
6. AUTHORS Athanasios J. Syllaos, Christopher L. Littler, Vincent C. Lopes, Usha Philipose, Oliver Chyan			5d. PROJECT NUMBER		
			5e. TASK NUMBER		
			5f. WORK UNIT NUMBER		
7. PERFORMING ORGANIZATION NAMES AND ADDRESSES University of North Texas 1155 Union Circle #305250 Denton, TX 76203 -5017			8. PERFORMING ORGANIZATION REPORT NUMBER		
9. SPONSORING/MONITORING AGENCY NAME(S) AND ADDRESS (ES) U.S. Army Research Office P.O. Box 12211 Research Triangle Park, NC 27709-2211			10. SPONSOR/MONITOR'S ACRONYM(S) ARO		
			11. SPONSOR/MONITOR'S REPORT NUMBER(S) 58295-EL.6		
12. DISTRIBUTION AVAILABILITY STATEMENT Approved for Public Release; Distribution Unlimited					
13. SUPPLEMENTARY NOTES The views, opinions and/or findings contained in this report are those of the author(s) and should not be construed as an official Department of the Army position, policy or decision, unless so designated by other documentation.					
14. ABSTRACT The objective of this program is to investigate the mechanisms of electrical conduction in amorphous silicon and identify factors affecting the performance of uncooled imaging focal plane array systems based on amorphous silicon microbolometer thermal detector structures. Measurements of the temperature dependence of conductivity and noise show that the dominant conduction mechanism in p-type a-Si:H is that of Mott variable range hopping. The hopping parameters are controlled by the film deposition conditions such as hydrogen dilution of the silane precursor and boron dopant level. The low frequency noise has a weak temperature dependence and is dominated					
15. SUBJECT TERMS Amorphous silicon, Temperature Coefficient of Resistance, TCR, 1/f Noise, Variable Range Hopping, Raman Spectroscopy, Multiple Internal Reflection IR Spectroscopy, microbolometer					
16. SECURITY CLASSIFICATION OF:			17. LIMITATION OF ABSTRACT	15. NUMBER OF PAGES	19a. NAME OF RESPONSIBLE PERSON
a. REPORT UU	b. ABSTRACT UU	c. THIS PAGE UU			Athanasios Syllaos
					19b. TELEPHONE NUMBER 940-565-2412

Final Report

Analysis of Electrical Transport Mechanisms in Amorphous Silicon Relevant to Uncooled Microbolometer Technology

Abstract

1. Introduction

- 1.1 Program Objective and Approach
- 1.2 Uncooled microbolometer IR imaging technology
- 1.3 Amorphous silicon thin films

2. Hopping conduction

- 2.1 Electrical conductivity
- 2.2 Temperature coefficient of resistance (TCR)
- 2.3 Noise in hopping conduction

3. Conductivity and TCR measurements and results

- 3.1 Materials and test devices
- 3.2 Conductivity and TCR results
- 3.3 Noise measurements and results

4. Optical characterization

- 4.1 Raman measurements and results
- 4.2 Multiple Internal Reflection Fourier Transform Infrared (MIR-FTIR) Spectroscopy

5. Summary

6. Bibliography

Final Progress Report 58295-EL

ABSTRACT

The objective of this program is to investigate the mechanisms of electrical conduction in amorphous silicon and identify factors affecting the performance of uncooled imaging focal plane array systems based on amorphous silicon microbolometer thermal detector structures. Measurements of the temperature dependence of conductivity and noise show that the dominant conduction mechanism in p-type a-Si:H is that of Mott variable range hopping. The hopping parameters are controlled by the film deposition conditions such as hydrogen dilution of the silane precursor and boron dopant level. The low frequency noise has a weak temperature dependence and is dominated by a $1/f$ component which follows the Hooge model and is correlated to the conductivity hopping parameters and in turn to the temperature coefficient of resistance (TCR). At high temperatures there is a generation-recombination (G-R) noise component. Raman spectroscopy measurements show that, with an increase of hydrogen dilution and/or growth temperature, both short and mid-range order improve, whereas the addition of boron results in the degradation of short range order. Multiple Internal Reflection IR spectroscopy of boron – hydrogen bonding in amorphous silicon shows B-H bonding configurations only. The B-H bonds can form electrically active fourfold coordinated bonding with silicon.

1.0 Introduction

This is the final progress report for Proposal Number: 58295-EL, Agreement Number: W911NF-10-1-0410, “Analysis of Electrical Transport Mechanisms in Amorphous Silicon Relevant to Uncooled Microbolometer Technology”. It describes the progress on the program for the entire performance period, beginning August 23, 2010 and ending on August 22, 2015.

1.1 Program Objective and Approach

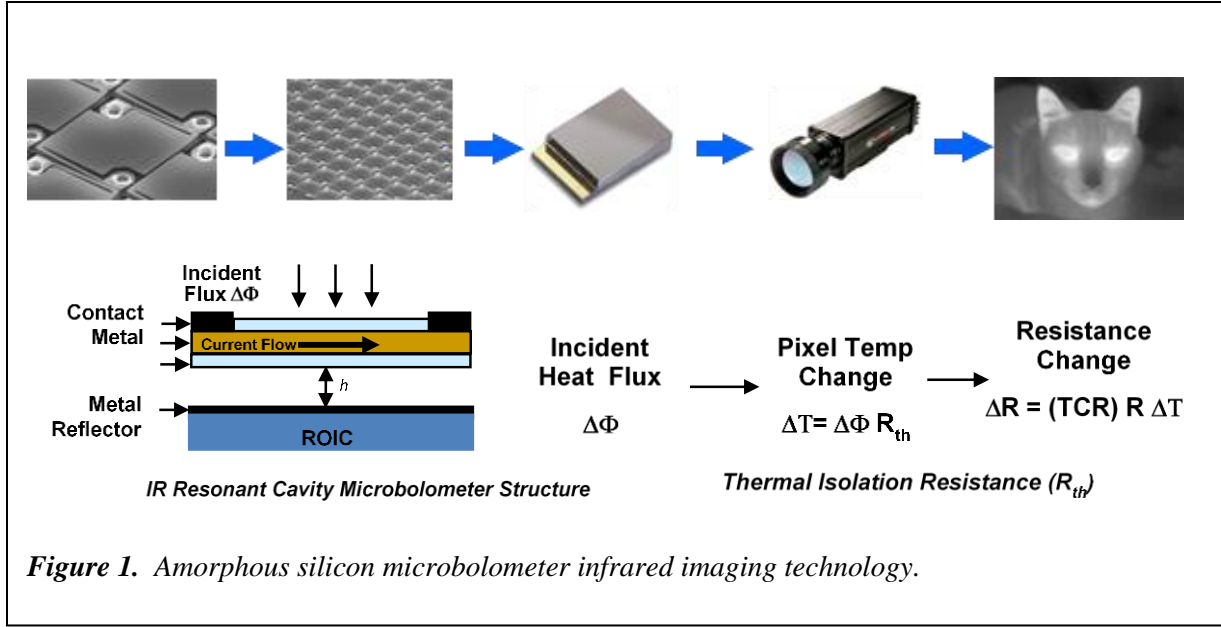
The objective of this program was to investigate electrical conduction mechanisms in amorphous silicon and identify factors affecting the performance of uncooled focal plane array imaging systems. The scientific barriers to overcome were comprehending the effects of dopants and hydrogen incorporation on the atomic structure and subsequent electrical transport properties.

The approach was to conduct comprehensive measurements of the temperature dependence of conductivity and noise to identify the effects of growth parameters on conduction mechanisms. Raman and Multiple Internal Reflection (MIR)-IR spectroscopy measurements were also performed to understand the influence of hydrogen and boron on the structural and chemical bonding properties of hydrogenated amorphous silicon (a-Si:H). Analysis of the results from these measurements was used to study the interdependencies of the measured properties and make correlations among them to identify and quantify the mechanisms of electrical transport in amorphous silicon.

1.2 Uncooled microbolometer IR imaging technology

Microbolometer arrays consist of a focal plane of pixels that are suspended above an integrated circuit and thermally isolated through the use of extremely narrow legs as shown in **Figure 1**. The pixels consist of a suspended membrane structures with an electrically active layer that changes in resistance as the pixel changes temperature. Infrared flux, $\Delta\Phi$, from a scene is focused on the array and causes the pixels to heat up by ΔT proportional to the IR flux incident upon the pixels and the thermal conductance G_{th} of each pixel. The integrated circuit below the pixels measures the change in resistance ΔR and generates a composite thermal image of the entire scene generated by the array.

The specific material properties required for application of a-Si:H films in microbolometer array technology are determined by the design requirements of the detector arrays and readout



electronics. The figures of merit describing the performance of a microbolometer based infrared camera are the noise equivalent temperature difference, NETD, and the thermal time constant of the camera detector array and electronics. The NETD of an Infrared camera at an ambient temperature T_o is defined as the ratio of temporal noise $Noise(T_o)$ to the change of the camera output signal $\Delta V_{out}(T_o)$ due to change in the scene temperature ΔT_{scene} [1]

$$(NETD)_{T_o} = \frac{Noise(T_o)}{\left(\frac{\Delta V_{out}(T_o)}{\Delta T_{scene}}\right)} \quad \text{Eq. 1}$$

In terms of detector parameters NETD is given by Eq. 2

$$(NETD)_{T_o} = \frac{Noise(T_o)}{\left(\frac{TCR \cdot (\beta \cdot \epsilon \cdot A_{det}) \cdot V_{det}}{G_{th}(k)}\right)_{T_o}} \quad \text{Eq. 2}$$

where, for the detector pixel, β is the fill factor, ϵ is the emissivity, A_{det} is the area, V_{det} is the detector bias voltage, and TCR is the thermal coefficient of resistance:

$$TCR = \frac{1}{R} \frac{dR}{dT} \quad \text{Eq. 3}$$

$G_{th}(k)$ is the thermal conductance of the microbolometer pixel. $G_{th}(k)$ is determined by the geometry of the pixel supporting “legs” that provide thermal dissipation pathways and the thermal conductivity, k , of the leg material(s).

Another figure of merit for microbolometers is the pixel thermal time constant, τ_{th} ,

$$\tau_{th} = \frac{C_p m}{G_{th}(k)} \quad \text{Eq. 4}$$

where C_p is the pixel materials specific heat, and m is the pixel mass.

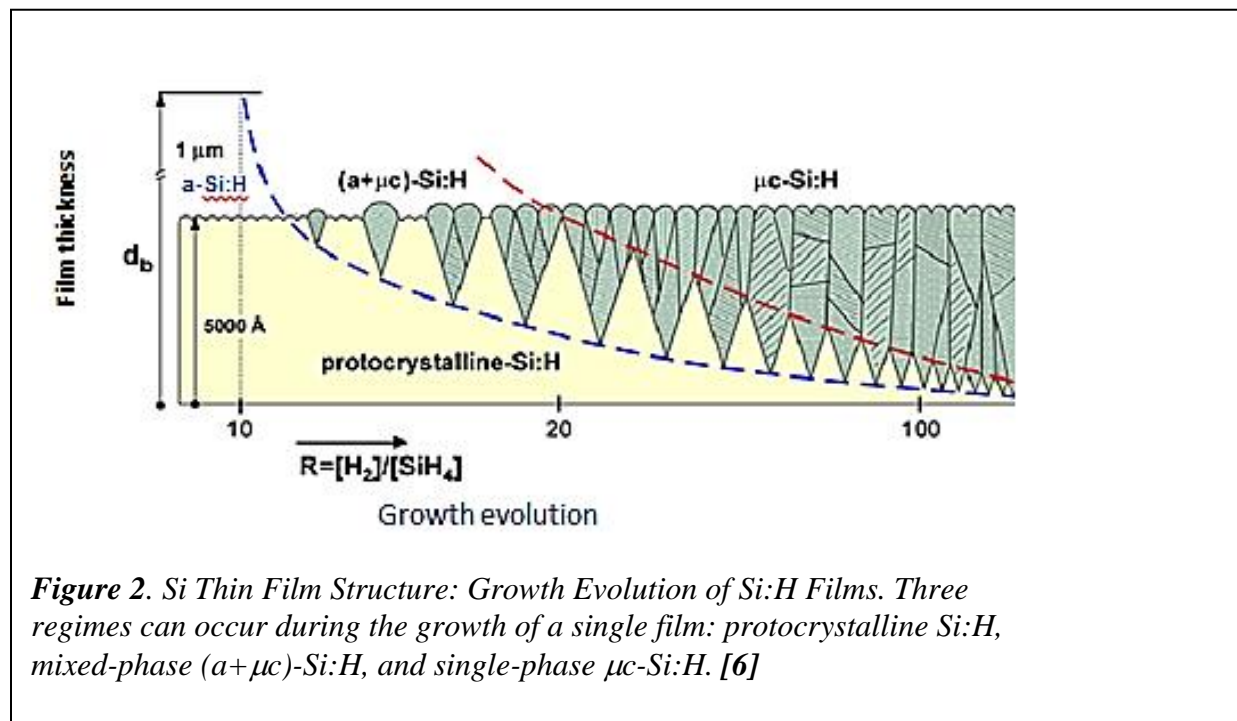
In general, high temperature coefficient of resistance (TCR) with low noise is desired at a conductivity dictated by the IC design to minimize NEDT. Selecting a resistance range determines the required a-Si:H resistivity for a specific pixel area and thickness. Generally, low mass, thin films are required to obtain low thermal time constant, setting an upper thickness limit. The low thickness or volume limit is determined by the noise requirements since low noise is associated with low resistivity and large pixel volume i.e., large number of carriers (Hooge's noise model). To a certain extent, the transport properties of a-Si:H are interdependent: higher resistivity a-Si:H exhibits higher TCR and noise.

1.3 Amorphous silicon thin films

Thin amorphous silicon (a-Si) films are widely used in several applications including solar cells and thin film transistors (TFTs) [2] as well as uncooled microbolometer infrared imaging arrays [3,4]. Advantages of a-Si films in device fabrication include: compatibility with silicon IC and MEMS manufacturing, well established low temperature deposition technologies, good interface properties with insulators, and the ability to be finely patterned with photolithographic technology well below the submicron level.

In a-Si, silicon atoms are bonded to four neighboring silicon atoms and form a random network. Some atoms are bonded to fewer than four neighbors and have dangling bonds (DB) $\sim 10^{19} \text{ cm}^{-3}$. Dangling bonds are defects and can be passivated with hydrogen and reduced to $\sim 10^{15} \text{ cm}^{-3}$. In almost all applications amorphous silicon is hydrogenated (a-Si:H). Silicon films exhibit a wide range of electrical and structural properties [5].

As shown in **Figure 2**, a powerful technique to affect the structure and material properties of silicon and the corresponding alloy films is the dilution of precursor reactants with hydrogen, $R_H = [H_2]/[SiH_4]$ [6]. An increase in H-dilution (R_H) results in a transition from amorphous to microcrystalline material. The amorphous to microcrystalline phase boundary depends both on



the dilution ratio R_H and the thickness of the film. As the thickness increases, ordered regions grow. The transition from amorphous to amorphous and microcrystalline (a+ μ C) is indicated by the dashed blue line and the transition from (a+ μ C) to microcrystalline (μ C) transition by the dashed red line. Thus, a variety of phases can be present in a-Si:H thin films and the presence of each will modify the electrical conduction properties. For the investigations reported here, care is taken to grow thin films near the amorphous to (a+ μ C) transition, where the samples are almost completely amorphous.

Excess hydrogen in the reactant gases passivates dangling bond defects and improves the atomic structure and electrical transport properties. Also, a-Si:H films can be doped with the same donors and acceptors as crystalline silicon: Boron for p type; Phosphorous or Arsenic for n-type [7]. In this report, the effects of hydrogen dilution and doping level on the conductivity and noise properties of p-type a-Si:H are described.

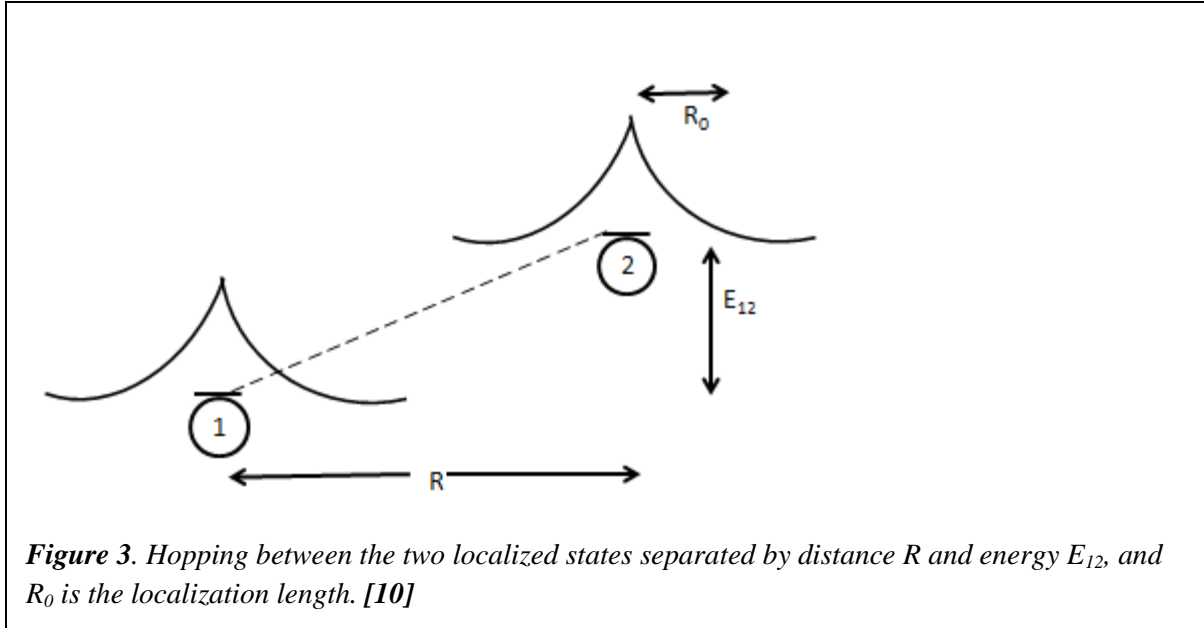
2.0 Hopping Conduction

2.1 Electrical Conductivity

In hydrogenated amorphous silicon (a-Si:H), electric transport can take place through extended states in the conduction band, valence band and states in the mobility gap. Near the Fermi energy, if the states are localized, the probability “P” that carriers ‘jump’ from one localized state to another localized state of higher energy depends on three factors [8]. These are (a) the attempt frequency ν (ph), which occurs in range of 10^{12} - 10^{13} s⁻¹ (b) the wave function of the electron and (c) the probability of finding a phonon with excitation energy (w) large enough to accomplish the hop. The probability rate of an electron jump is given by,

$$P = \nu(ph)e^{-2\alpha R}e^{-w/kT} \quad \text{Eq. 5}$$

where $\xi = 1/\alpha$ is the decay length of localized wave function, R is the spatial distance between the two hopping sites, w is the energy difference between two states, and k is the Boltzmann



constant. From the product of α and R the hopping conductivity can result from Nearest Neighbor Hopping (NNH) or Variable Range Hopping (VRH). The energy levels of a p-type semiconductor are affected by potential fluctuation. Charge carriers hop from one to another site with the assistance of a phonon. The most probable form of hopping is between nearest neighbor atoms and is designated NNH. The temperature dependence of conductivity due to NNH is similar to that of thermal activation, where the magnitude of activation energy corresponds to the potential fluctuation. They have similar temperature dependence (i.e., the characteristic exponent (“ p ”)=1) though the conduction mechanism is different. Depending on the energy of the carrier, it can migrate from one site to another site at various distances, and the resulting conductivity will deviate from NNH to VRH. The NNH conduction is expected if $\alpha R_0 \gg 1$ where R_0 is the average distance to the nearest neighbor. If $\alpha R_0 \leq 1$, VRH is expected. The hopping distance R increases with decreasing temperature [8]; as a result, NNH is expected to dominate at higher temperatures and VRH at lower temperatures. The hopping mechanism of electrical conduction corresponds to low mobility as the carrier jumps are associated with a weak overlap of the wave functions. As a result, the conductivity has an exponential dependence with temperature [9].

Figure 3 shows the carrier hopping between the two states separated by the distance R and energy E_{12} [10]. Using Einstein’s relation,

$$\text{Mobility, } \mu = \frac{eD}{kT} \quad \text{Eq. 6}$$

where,

$$\mu = \frac{PR^2}{6} . \quad \text{Eq. 7}$$

The conductivity can be written as,

$$\sigma = (1/6)e^2PR^2 N(E_F). \quad \text{Eq. 8}$$

Here $N(E_F)$ is the DOS at Fermi level and $N(E_F)kT$ is the number of charge carriers that are involved in the electrical conduction. Combining with Eq. 5, the conductivity can be written as,

$$\sigma = (1/6)e^2R^2v_{ph} N(E_F)\exp(-2\alpha R)\exp(-W/kT) \quad \text{Eq. 9}$$

With a decrease in temperature, the number and energy of phonons decreases and more energetic phonon-assisted hops become less favorable. Carriers will try to hop larger distances to get to sites that lie energetically closer than the nearest neighbors, resulting in a variable range for the hopping distance between traps. The exponential term $\exp(-2\alpha R - W/kT)$ will not have its maximum value for the nearest neighbor. Mott used an optimization procedure to get the most probable hopping distance. If the density of states (DOS) is expressed in units of volume per unit energy $N(W)$, then the possible number of states within the ΔW in a distance R from particular atom is given by, $\left(\frac{4\pi}{3}\right)R^3N(W)W$. The charge carrier can leave its original site if there exists at least one vacancy or site for its hop, and in such case the average energy spacing between the states in the vicinity of the Fermi level is,

$$W = \left(\frac{3}{4\pi}\right)\frac{1}{R^3N(E_F)} \quad \text{Eq. 10}$$

And, the jump probability is,

$$P = v_{ph}\exp(-2\alpha R - \frac{3}{4\pi R^3 N(E_F)kT}) \quad \text{Eq. 11}$$

The most probable jump distance is found by minimizing the exponent as a function of R given by,

$$R = \left\{\frac{9}{8\pi\alpha N(E_F)kT}\right\}^{0.25} \quad \text{Eq. 12}$$

The general expression for a hopping mechanism (obtained from the hopping probability) can be written as,

$$\sigma = \sigma_o e^{-\left(\frac{T_o}{T}\right)^p} \quad \text{Eq. 13}$$

where σ_o is the conductivity prefactor, T_0 is the characteristic temperature and “ p ” is a characteristic exponent that distinguishes between various conduction mechanisms. As the hopping conduction of charge carriers occurs between the localized states in the vicinity of the Fermi level (E_F), the details of the DOS, in the vicinity of E_F , is an important consideration in the determination of the temperature dependence of conductivity. Mott considered a constant DOS in the vicinity of the E_F and determined the value of $p = 1/4$ for a three dimensional system. However, Efros and Skhlovskii [9] considered the long range Coulomb interaction and found that it reduces the DOS to zero at the Fermi level, thereby creating a so-called “Coulomb gap (CG)” at low enough temperatures. This form of hopping conductivity results when an electron migrates from one site to another site leaving a positively charged vacancy. For hopping to occur, the electron must have sufficient energy to overcome this Coulomb interaction between the electron and the ‘hole’; and thus, a “Coulomb gap”, defined by this interaction, appears. The temperature dependence of conductivity, which can be described by Eq. 13, is still valid, but the characteristic exponent now becomes $p = 1/2$ in this case.

Mott [8] neglected the long-range Coulomb interaction and assumed that the DOS was a constant at the Fermi energy. In general, the DOS, $N(E) \sim (E-E_F)^n$. For the Mott hopping conduction, $n = 0$ and the DOS is constant, yielding an expression for the conductivity of the form of Eq. 13 with $p = 1/4$. For ES conduction, $n = 2$, and yields an expression for the conductivity of the form of Eq. 13 with $p = 1/2$. For large value of n , $p \sim 1$ in the Eq. 13 and corresponds to NNH conduction. Each of these hopping mechanisms and their range of validity will be briefly discussed below.

a) When the power $p = 1/4$, the conduction mechanism is described by the Mott [8] model

$$\sigma_M = \sigma_{oM} e^{-\left(\frac{T_{oM}}{T}\right)^{\frac{1}{4}}} \quad \text{Eq. 14}$$

where T_{oM} is the Mott characteristic temperature given by,

$$T_{oM} = \frac{\beta}{kN(E_F)\xi^3} \quad \text{Eq. 15}$$

Here, $N(E_F)$ is the density of states at the vicinity of the Fermi level, k is the Boltzmann constant and $\beta = 18$.

For the Mott theory to be valid, the charge carrier must “hop” an average distance that is considerably more than the nearest neighbor trap separation and considerably greater than the localization length “ ξ ”.

Using the expression for T_{oM} as shown above, an equation for the hopping distance and hopping energy are given, respectively as [11],

$$R_{hop,M} = \frac{3}{8} \left(\frac{T_{0M}}{T} \right)^{0.25} * \xi \quad \text{Eq. 16}$$

And,

$$\Delta_{hop,M} = \frac{1}{4} (kT) \left(\frac{T_{0M}}{T} \right)^{0.25} \quad \text{Eq. 17}$$

Correlations with the values of the hopping distance and energy obtained for samples differing in doping and H-dilution will be given in the results section of this section.

b) For the power $p = 1/2$, the conductivity equation results from the Efros-Shklovskii-VRH [9] which is,

$$\sigma_{ES} = \sigma_{0ES} e^{-\left(\frac{T_{0ES}}{T} \right)^{\frac{1}{2}}} \quad \text{Eq. 18}$$

where σ_{0ES} is the prefactor and T_{0ES} is the characteristic temperature for the ES-VRH given by,

$$T_{0ES} = \frac{\beta' e^2}{k \varepsilon \xi} \quad \text{Eq. 19}$$

with $\beta' = 2.8$ and ε is the dielectric constant of the medium, ξ is the localization length [12].

For the ES theory, the average hopping distance must be greater than the nearest neighbor distance and greater than the localization length. In this case, when the Fermi energy lies in a range of energies where the states are localized, the Coulomb interaction results in a zero in the density of states at the Fermi level that leads to the formation of a Coulomb Gap (CG) [11][13]. The appearance of the CG by electron correlations can be considered the minimum energy required for a hopping conduction process to occur between the localized states with finite energy and spatial distribution [9] [14].

c) When $p = 1$, the conductivity can be expressed as,

$$\sigma = \sigma_o e^{-\left(\frac{T_o}{T} \right)} \quad \text{Eq. 20}$$

The conduction results from hopping between nearest neighbor sites, referred to as the nearest neighbor (NNH) model

When $p = 1$, the conductivity can be expressed as

$$\sigma = \sigma_o e^{-\left(\frac{T_{0NNH}}{T} \right)} \quad \text{Eq. 21}$$

The conduction results from hopping between nearest neighbor sites referred to as the nearest neighbor hopping (NNH) model. In the NNH case, T_{0NNH} , is related to the energy of the Coulomb interaction on the mean distance between localized states (traps), d .

$$T_{0NNH} = \beta'' \frac{e^2}{k\epsilon d} \quad \text{Eq. 22}$$

In most materials the coulomb gap is small, and Efros-Shklovskii type conductivity is observed only at low temperature. For intermediate temperatures, there is a crossover from Efros-Shklovskii to Mott conduction, and, at high temperatures, both the Mott and Efros-Shklovskii transition to Nearest Neighbor conduction. The temperature where the crossover occurs, T_{cross} , is given by [11]

$$T_{\text{cross}} = \frac{16T_{0ES}^2}{T_{0M}} = \frac{5.9e^4 N(E_F)\xi}{\epsilon^2 k_B} \quad \text{Eq. 23}$$

Substitution of T_{0M} and T_{0ES} in Eq. 23 yields the Mott to Efros-Shklovskii crossover temperature in terms of the density of states $N(E_F)$, given by

$$T_{\text{crossM} \rightarrow \text{ES}} = \frac{5.9e^4 \xi}{\epsilon^2 k_B} N(E_F) \quad \text{Eq. 24}$$

The Mott to NNH crossover occurs when the hopping distance R_{hopM} approaches the nearest neighbor distance d , given by

$$R_{\text{hopM}} = \frac{3}{8} \left(\frac{T_{0M}}{T_{\text{cross}}} \right)^{\frac{1}{4}} \xi = d \quad \text{Eq. 25}$$

Substituting T_{0M} in Eq. 25 yields the Mott to NNH crossover temperature in terms of the density of states $N(E_F)$.

$$T_{\text{crossM} \rightarrow \text{NNH}} = \left(\frac{3}{8} \right)^4 \frac{18}{k_B} \frac{\xi}{d^4} \frac{1}{N(E_F)} \quad \text{Eq. 26}$$

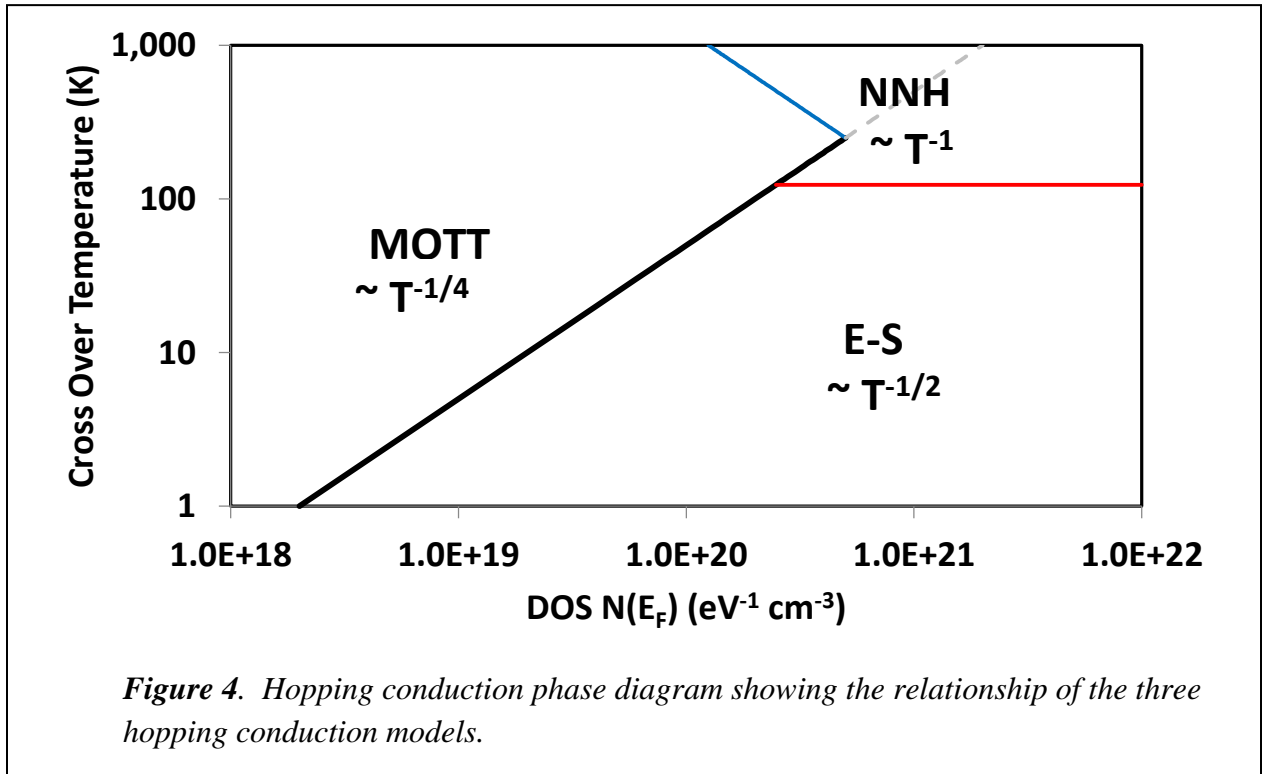
The Efros-Shklovskii to NNH crossover occurs when the hopping distance R_{hopES} [9] approaches the nearest neighbor distance d .

$$R_{\text{hopES}} = \frac{1}{4} \left(\frac{T_{0\text{ES}}}{T_{\text{cross}}} \right)^{\frac{1}{2}} \xi = d \quad \text{Eq. 27}$$

Substituting $T_{0\text{ES}}$ in Eq. 27 yields the Efros-Shklovskii to NNH crossover temperature. In this case the cross over temperature is not directly dependent on the density of states $N(E_F)$.

$$T_{\text{crossES} \rightarrow \text{NNH}} = \left(\frac{1}{4} \right)^2 \frac{2.8}{k_B \epsilon} \frac{\xi}{d^2} \quad \text{Eq. 28}$$

Figure 4 shows a qualitative plot of the crossover temperature vs the density of states at the



Fermi level $N(E_F)$ for a typical localization length $\xi = 2 \text{ \AA}$, for a dielectric constant $\epsilon = 11$, and trap nearest neighbor distance $d = 10 \text{ nm}$. Shown are the crossover temperatures for the three transitions: ES to Mott, Mott to NNH, and ES to NNH as described by Eq. 24, Eq. 26, and Eq. 28 respectively.

A variety of materials exhibit hopping conduction. These include disordered semiconductors, such as organic semiconductors, nanomaterials, and biomaterials. Examples of such materials and the type of hopping conduction they exhibit are shown below.

1. Amorphous (Disordered Materials)

- p-type a-Si:H (ES→Mott) [15]
- n-type a-Si:H (ES→NNH) [16]
- VO_x (ES) [17]
- TiO₂ (ES→Mott) [18]
- In_xO_y (ES→Mott) [19]
- Amorphous HgCdTe (Mott) [20]

2. Nanomaterials

- PbSe Nanocrystals (ES→NNH) [21]
- CdSe Quantum Dots (ES→Mott) [22]
- Hydrogenated Graphene (ES) [23]
- Carbon Nanotubes (Mott) [24]

3. Organic Semiconductors

e.g.P3HT (2D Mott, p=1/3) [25]

4. Bio-materials

DNA (Mott→NNH) [26,2]

2.2 Temperature Coefficient of Resistance (TCR)

The TCR is a measure of the rate at which the conductivity changes with temperature. For certain applications, such as a bolometric sensor, the TCR is a figure of merit, because an increase in the TCR correlates with an increase in the bolometric response. The nature of the TCR can be understood and described by the specific mechanisms controlling electrical conduction.

The TCR is defined as [28],

$$|TCR| = \left| \frac{1}{\sigma} \frac{d\sigma}{dT} \right| \quad \text{Eq. 29}$$

where σ is the conductivity of the material at temperature T.

For a conductivity described by Eq. 13, the general equation connecting the TCR with the power “ p ” is given by,

$$|TCR| = \left| \frac{1}{\sigma} \frac{d\sigma}{dT} \right| = p \frac{T_0^p}{T^{p+1}} \quad \text{Eq. 30}$$

It is sometimes convenient to write the Eq. 30 in the following form,

$$\left(\frac{T_0}{T} \right)^p = -\frac{T}{p} TCR \quad \text{Eq. 31}$$

where the values of p lie between 0 and 1.

For NNH, Eq. 30 becomes,

$$|TCR_{NNH}| = \frac{T_0}{T^2} \quad \text{Eq. 32}$$

In the case of the M-VRH, the value of $p = 1/4$, then TCR is given by,

$$|TCR_M| = \frac{1}{4} \left(\frac{T_{oM}}{T^5} \right)^{1/4} \quad \text{Eq. 33}$$

Similarly, the TCR for ES-VRH (with $p = 1/2$) is given by,

$$|TCR_{ES}| = \frac{1}{2} \left(\frac{T_{oES}}{T^3} \right)^{1/2} \quad \text{Eq. 34}$$

In terms of the conductivity and its prefactor σ_0 , the general TCR can be expressed as,

$$TCR = p \frac{1}{T} (\ln \sigma_0 - \ln \sigma) = p \frac{1}{T} (\ln(\rho \sigma_0)) \quad \text{Eq. 35}$$

This shows that the TCR is directly proportional to the resistivity.

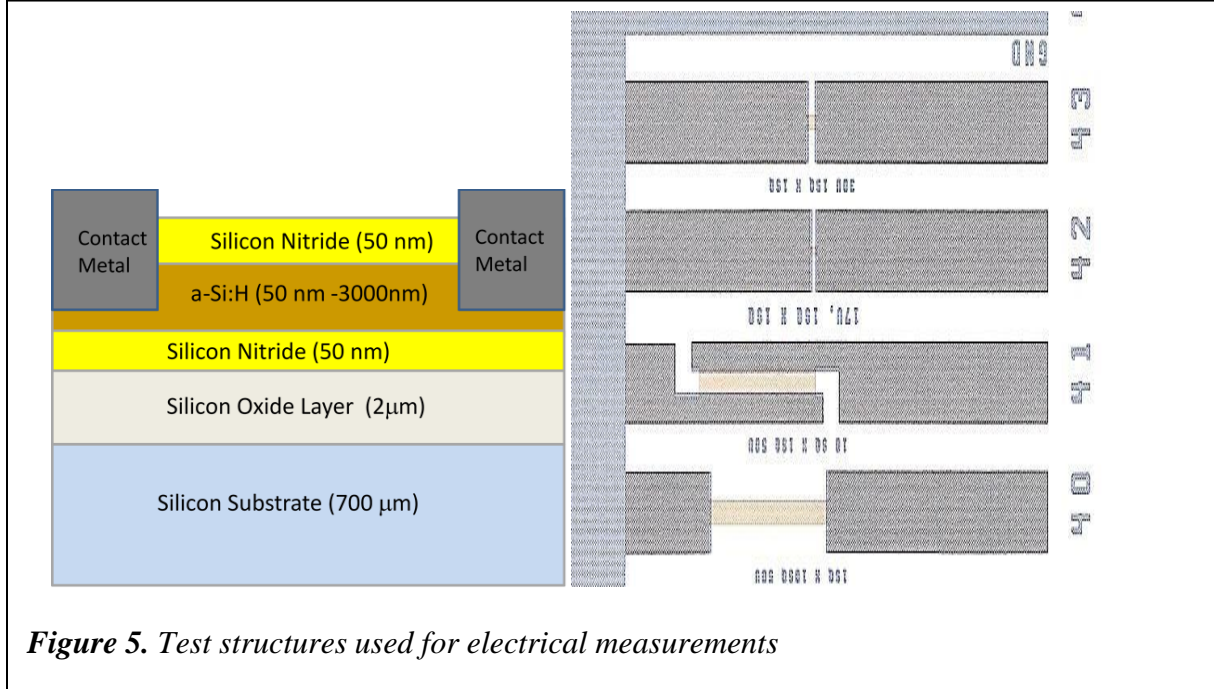
2.3 Noise in hopping conduction

Theoretical models for 1/f noise in variable range hopping conduction [29,30] show that 1/f noise at low temperature decreases with increasing temperature. These models also predict that 1/f noise increases with the characteristic temperature T_0 .

3.0 Conductivity and TCR measurements and results

3.1 Materials and test devices

Electrical measurements were performed on test resistor structures with varying aspect ratio to measure samples in a broad resistance range to evaluate surface effects and contact resistance.



The samples placed in a dark, cold-shielded cryostat to ensure isothermal measurements with the sample in thermal equilibrium. The amorphous silicon thin films were grown by PECVD using capacitively-coupled 13.56 MHz plasma with the substrate on the ground electrode. The growth temperatures for the samples studied were 275 C and 365 C. The source gases are silane (SiH_4) and hydrogen in Argon. The films were deposited on Si wafers with an insulating SiO_2 layer and a silicon nitride film Si_3H_4 layer as shown in **Figure 5**. The thickness of the a-Si: H layer range from approximately 500 Å to 3000 Å. The films were doped p-type by using boron trichloride (BCl_3) as a dopant precursor to incorporate boron in the thin films. The doping ratio is defined as $r = [\text{BCl}_3]/[\text{SiH}_4]$, and H-dilution as $R_H = [\text{H}_2]/[\text{SiH}_4]$. Standard photolithography techniques were used to prepare two, three and four terminal test structures. Metal contacts were made for electrical measurements. Samples from the wafer were die-attached onto ceramic carriers and wire-bonded for temperature dependent electrical measurements

3.2 Conductivity and TCR results

The conductivity versus temperature plot for samples representing a wide range of doping and H-dilution prepared at the growth temperature of 365 C is shown in **Figure 6**.

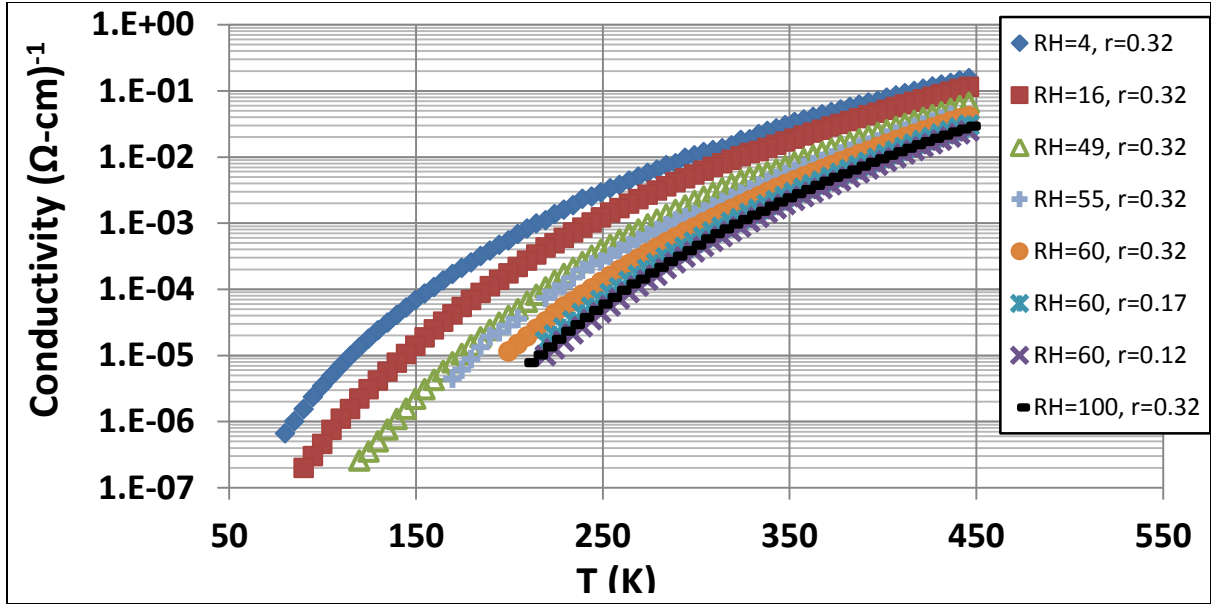


Figure 6. Temperature dependent conductivity of various samples differing in boron doping and H-dilution

The results shown indicate that the conductivity increases with the boron doping and decreases with increasing hydrogen (R_H). Samples with the lowest R_H and highest “ r ” have the highest conductivity. To better illustrate the effect of hydrogen on conductivity is shown in the **Figure 7**. This figure illustrates the decrease of conductivity with the increase of H-dilution for the highest doping ratio. More about the bonding energy between different elements will be discussed shortly.

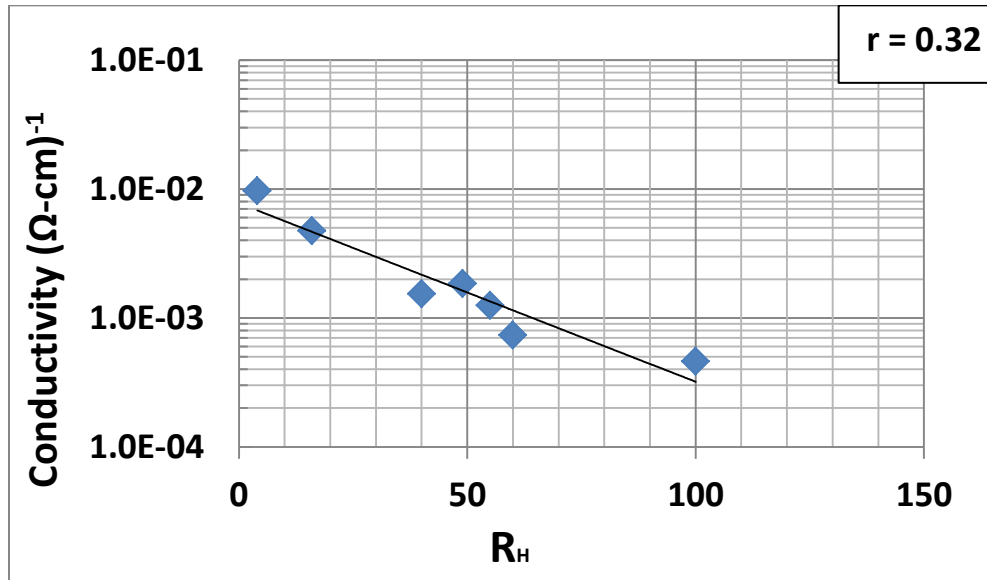


Figure 7. Room temperature conductivity vs. Hydrogen dilution R_H for fixed boron doping $r = 0.32$ (highest doping).

Figure 8 shows the experimental results obtained for samples having two different boron doping ratios ($r = 0.17$ and 0.32), two different dilutions ($R_H = 40$, and 55) and thickness close to 1000\AA .

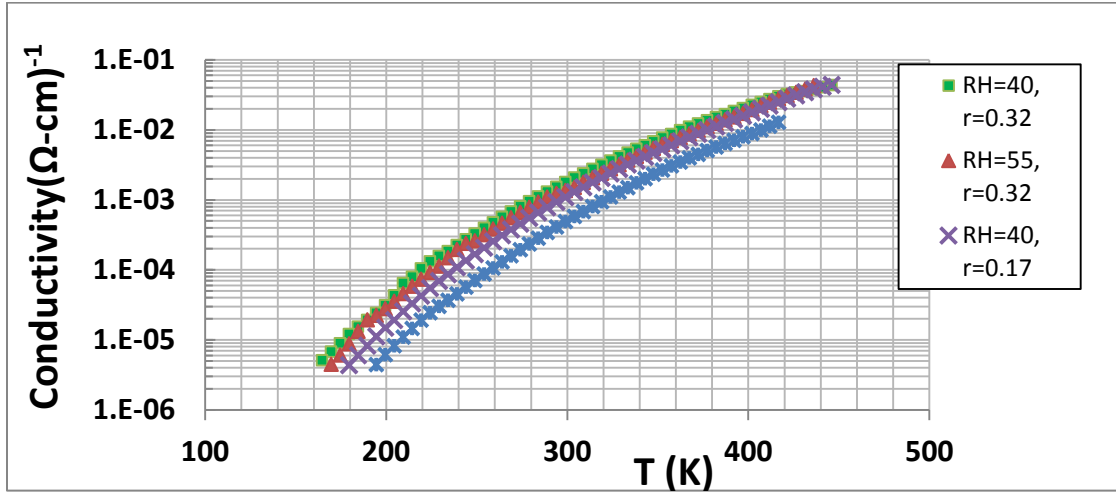


Figure 8. Conductivity of *a*-Si:H thin film ($\sim 1000\text{\AA}$ thick) for different Hydrogen dilution R_H and boron doping ratio r .

Figure 8 clearly shows that for a fixed dilution if the doping is increased the conductivity increases. Furthermore, for a fixed doping, if the R_H is increased the conductivity decreases. The room temperature resistivity values for these samples are in Table 1 below.

These general features due to hydrogen and boron incorporation can be described as follows: The band gap of *a*-Si increases with the increase of R_H due to the passivation of dangling bonds [31,32] which results in a decrease in conductivity. The band gap increases results from the introduction of hydrogen due to the formation of the higher bonding energy of the Si-H bond over that of the weaker Si-Si bonds. This effect is evident in *a*-Si grown by Glow discharge [32]. and reactively sputtered¹⁰ techniques and should be expected on PECVD-grown *a*-Si:H.

With the addition of boron there is an increase of conductivity due either to the activation of the boron substitutional acceptor in the *a*-Si:H matrix or by the “gettering” of hydrogen by boron forming a B-H bond, leading to the reduction of hydrogen available to passivate the dangling bonds. An increase in the number of Si-B bonding results in the increase of electrical conductivity due to reduction of the gap, because the Si-B bonding energy (2.1 eV) is smaller than Si-Si (2.2 eV) and Si-H (3.4 eV) bonding energies [33].

Figure 9 shows the experimental results of the samples with fixed H-dilution ($R_H = 60$) of three different levels of boron doping ($r=0.12$, 0.17 , and 0.32).

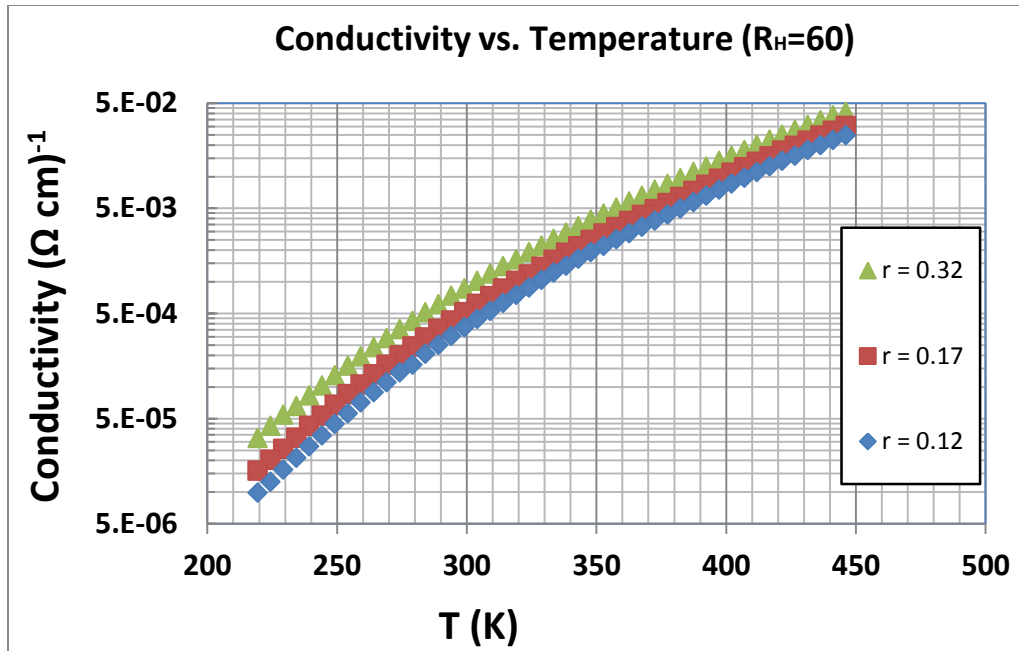
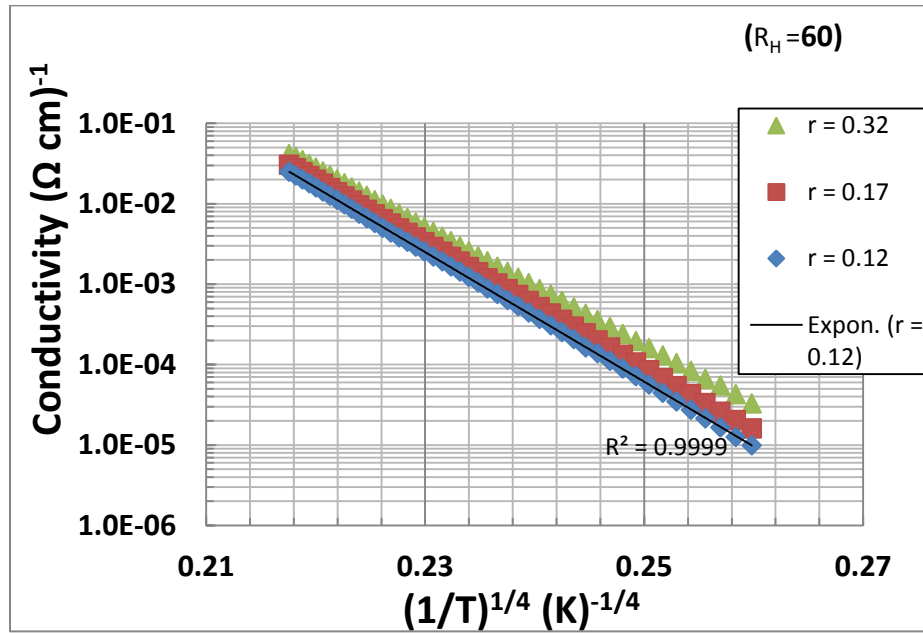
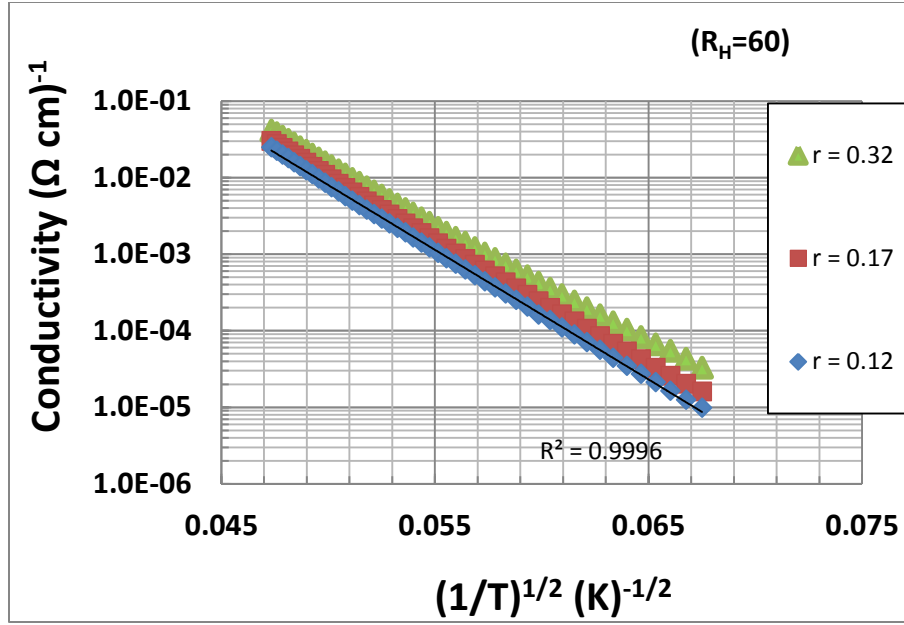


Figure 9. Conductivity of *a*-Si:H thin film (~ 500 Å thick) for fixed R_H and different boron doping

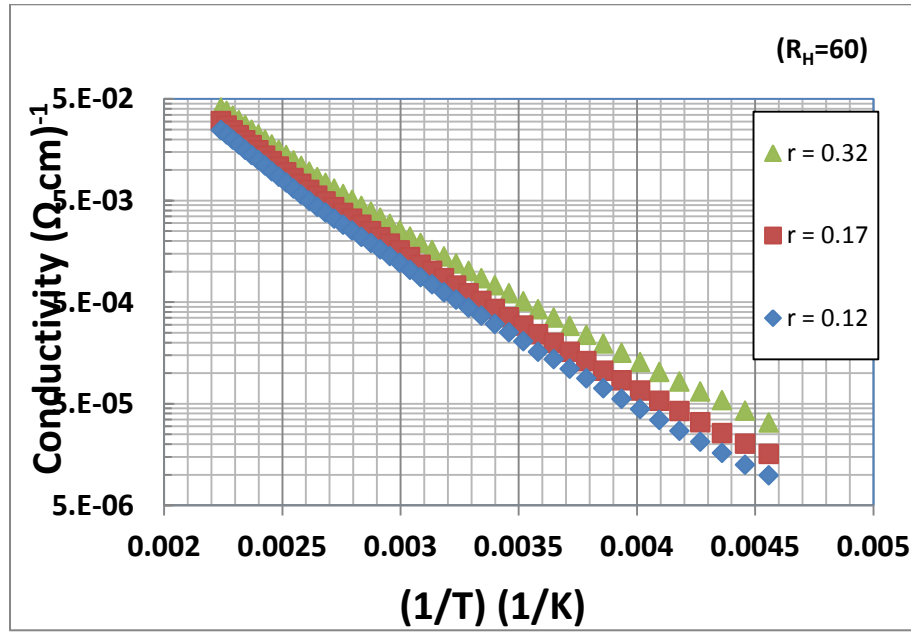
As mentioned earlier, the graph clearly shows that the conductivity increases with the increase of the boron concentration. To determine which conductivity mechanism dominates in these samples, the log of the conductivity versus $T^{-1/4}$, $T^{-1/2}$, and T^{-1} has been plotted in **Figure 10**.



(a)



(b)



(c)

Figure 10. (a) Log conductivity vs. $T^{-1/4}$ and (b) Log conductivity vs. $T^{-1/2}$ (c) Log conductivity vs. T^{-1} .

In order to determine the conduction mechanism, as shown in **Figure 10**, the Log conductivity vs. $T^{-1/4}$ and $T^{-1/2}$ are fit by the Mott and ES VRH conduction models. It is seen that

the Mott expression provides only a slightly better fit to the data points, as evidenced by the higher R^2 value. From the conductivity vs. $T^{-1/2}$ the R^2 value is 0.9996 and from conductivity vs. $T^{-1/4}$ the R^2 value is 0.9999. However, the difference in R^2 values is small, making it difficult to distinguish the best between the Mott and ES VRH models.

In order to better delineate which conductivity mechanism dominates, a Resistance Curve Derivative Analysis (RCDA) [34] method was performed on the data shown in **Figure 11**. This method allows one to extract the power value “ p ” directly from the analysis and thus the transport mechanism. In the RCDA method, the log of the conductivity data versus temperature is numerically differentiated, and the quantity “ w ”, is determined.

$$\text{where ,} \quad w = \frac{d(\log \sigma)}{d(\log T)} \quad \text{Eq. 36}$$

From Eq. 13, the quantity “ w ” can be expressed as,

$$w = p \left(\frac{T_0}{T} \right)^p \quad \text{Eq. 37}$$

The expression can be written in the straight line form as,

$$\log w = -p \log T + \log p (T_0)^p. \quad \text{Eq. 38}$$

comparing with straight line equation $y = mx+b$, the value “ p ” is obtained from the slope and the y- intercept value “ A ” can be used to get the characteristic temperature by using the equation,

$$T_0 = \left(\frac{10^A}{p} \right)^{\frac{1}{p}} \quad \text{Eq. 39}$$

Recalling the TCR relation with “ p ” and combining with the “ w ” we obtain a simple expression which, relates TCR and “ w ” with temperature.

$$TCR = \frac{w}{T} \quad \text{Eq. 40}$$

Figure 11 shows the plot of $\log w$ vs. $\log T$ for a representative sample.

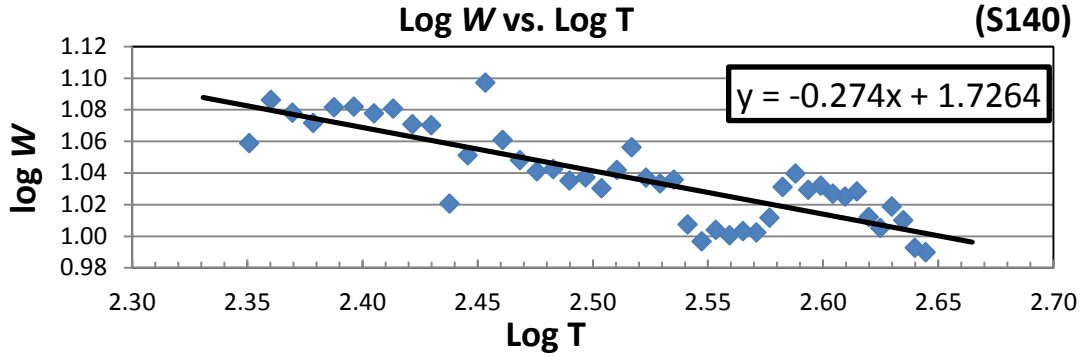


Figure 11. Illustration of the RCDA method.

By the RCDA method, for sample S-140 ($r = 0.12$) the “ T_0 ” and the “ p ” values are 1.1×10^9 K and 0.274 respectively. Similarly the “ T_0 ” and “ p ” values for S-143 ($r = 0.17$) are obtained as 1.0×10^9 K and 0.249 respectively and for the S-114 ($r = 0.32$) “ T_0 ” is 8.2×10^8 K and “ p ” is 0.249. **Figure 12** shows the results of the RCDA analysis for three samples with $R_H = 60$ having three different boron levels. The derived “ p ” values are also indicated by the slope of the linear fit.

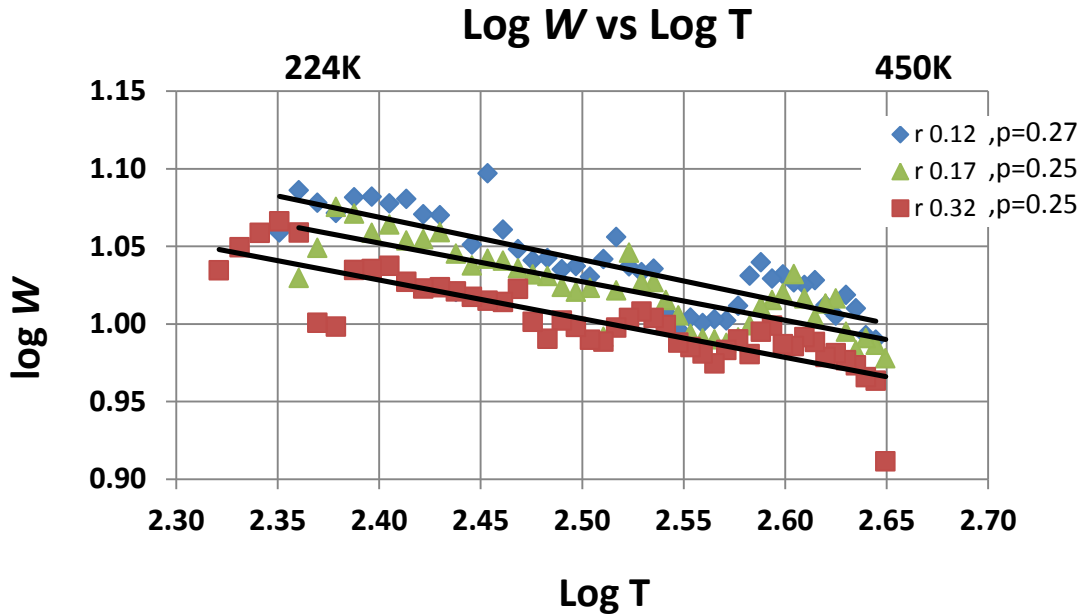


Figure 12. RCDA of $a\text{-Si:H}$ samples for fixed R_H and various doping levels.

Since all values of “ p ” are close to or equal to 0.25, the dominant conduction mechanism is the Mott-VRH in these samples. From Eq. 37 and Eq. 39 the TCR is a function of “ p ” as well.

As mentioned earlier, the TCR is determined by taking the derivative of conductivity data and dividing by the conductivity. For the set of samples the numerical derivative of the experimental values of the conductivity with respect to the temperature was performed and compared to the predictions of the Mott-TCR model in **Figure 13**. There is a good agreement between the experimental results and the model, further validating the Mott mechanism of conduction for these samples.

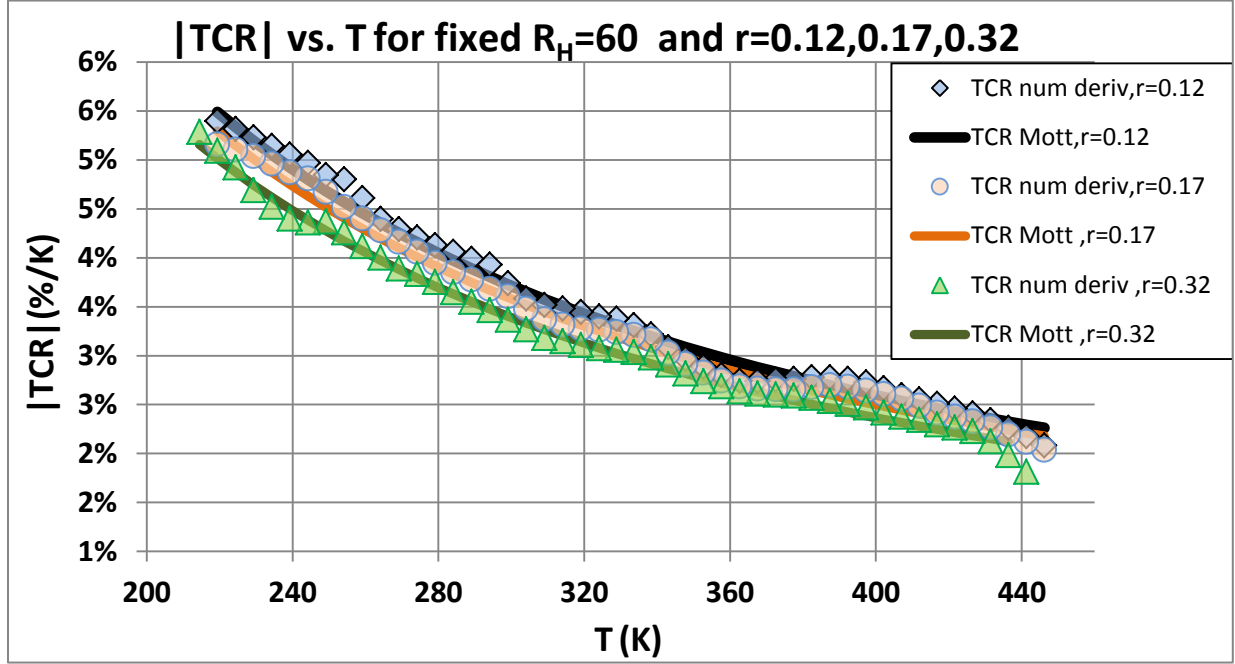


Figure 13. TCR of the samples with fixed R_H and three different “ r ” values.

Table 1 shows the Mott- parameters along with the TCR_Mott values at room temperature for the set of samples with fixed R_H and varying boron doping ratios

Table 1. Parameters determined by Mott-fitting of conductivity and TCR data at room temperature

ID	[" r "]	[R_H]	Thickness(Å)	RT Resistivity (Ω -cm)	σ_{0M} (Ω cm) ⁻¹	To(K)	TCR_Mott	Value of “ p ”
S140	0.12	60	523	3267	8.33E+15	1.10x10 ⁹	3.81	0.274
S143	0.17	60	521	2336	2.37E+15	1.02 x10 ⁹	3.68	0.249
S114	0.32	60	519	1360	4.10E+14	8.20 x10 ⁸	3.48	0.249

The table indicates that, with an increase of boron doping for fixed R_H , the TCR decrease as the Mott parameter decreases. Once the analysis has determined the conduction mechanism, the TCR can be predicted and compared to the TCR calculated from the temperature-dependent

conductivity data. That the values of “ p ” for various doping values are close to $\frac{1}{4}$ indicates that the mechanism is according to the Mott-VRH. Comparing the values obtained by RCDA method within the **Table 1**, it can be clearly seen that the “ p ” values are in excellent agreement and the power values are very close to $\frac{1}{4}$ in this set of samples, confirming that the conduction mechanism is the M-VRH in the temperature range studied (~ 200 K-450 K). Further, the TCR values by numerical differentiation and the TCR_Mott are in reasonable agreement as shown in the **Figure 13**.

At low temperatures, the conductivity is seen to deviate from M-VRH as shown in **Figure 14**, for a low dilution, highly doped sample, indeed indicate that the conductivity deviates from solely M-VRH conductivity. The conductivity can be described in terms of a combination of M-VRH and ES-VRH, where the total conductivity is given by $\sigma = \sigma_M + \sigma_{ES}$.

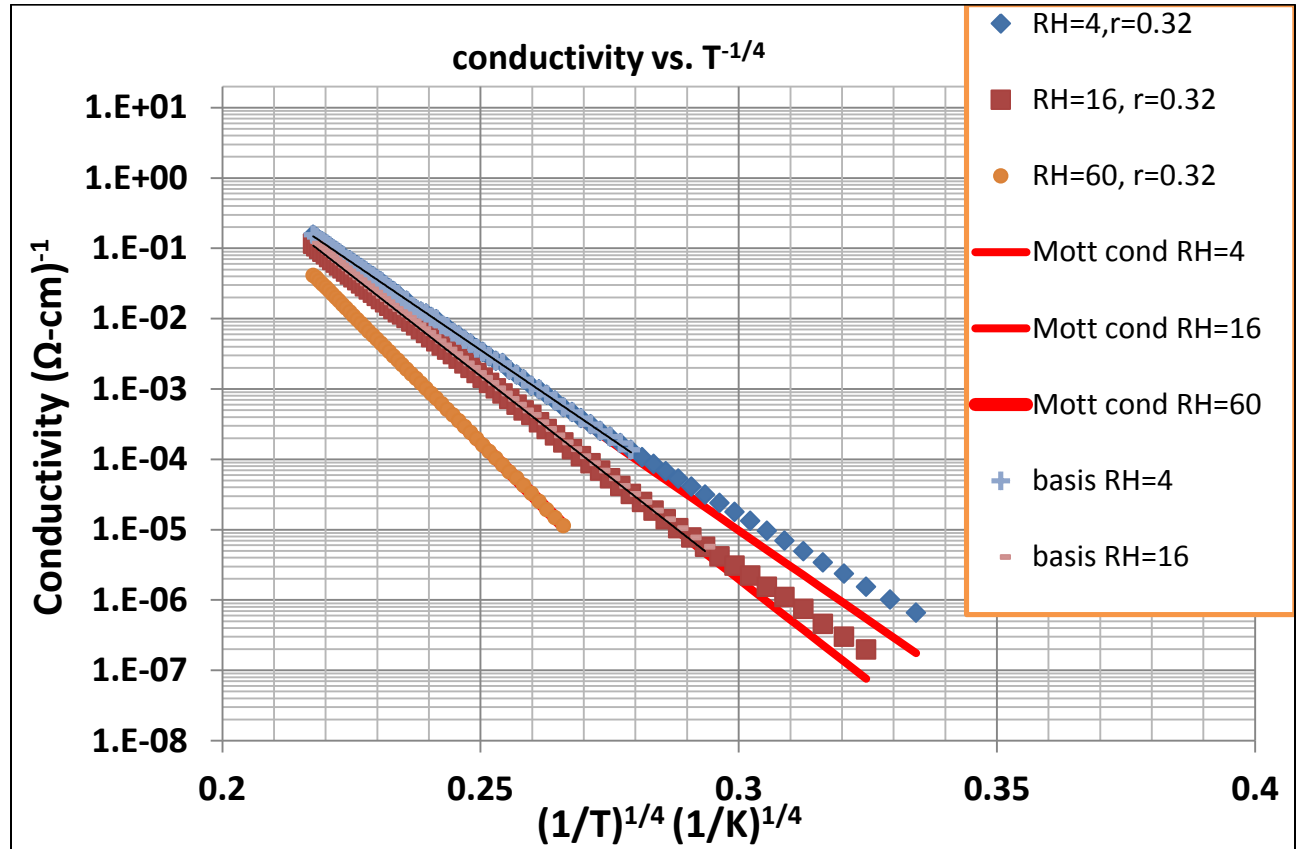


Figure 14. Conductivity vs. $T^{-1/4}$.

The results of the analysis are shown in **Figure 15** and **Figure 16**. Each shows contributions from both the M-VRH and the ES-VRH, as represented by the blue line and the black lines respectively. The red line is the sum of the Mott and the ES conductivities and shows the fit to the data points. The derived conductivity parameters are tabulated in **Table 2**.

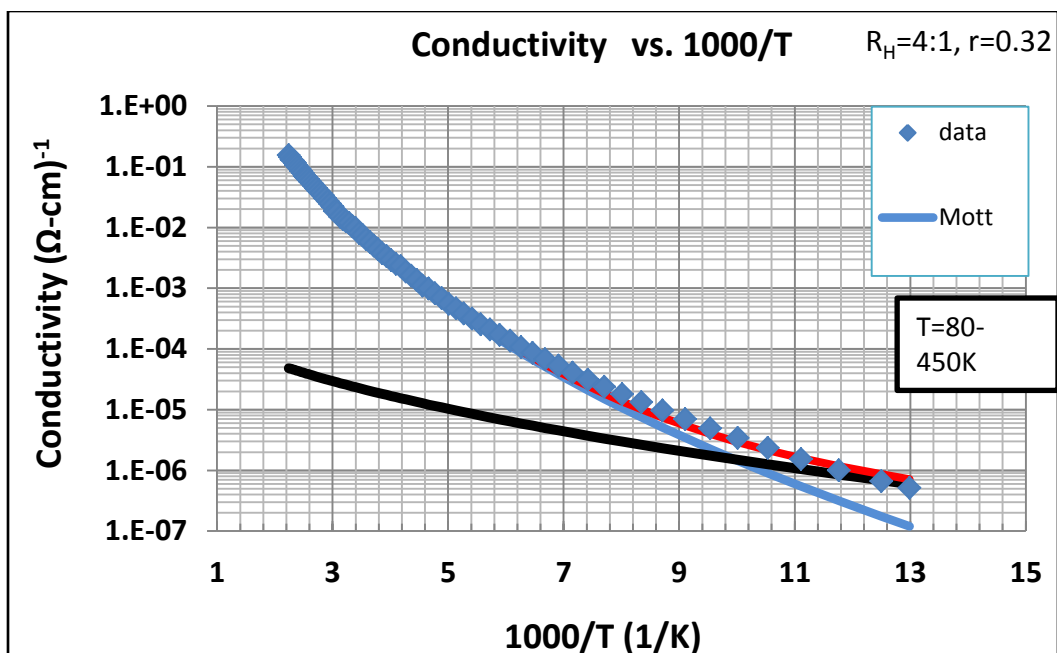


Figure 15. Temperature dependent conductivity for $R_H = 4$, showing the contributions of Mott and ES conductivity and the fit to the experimental results.

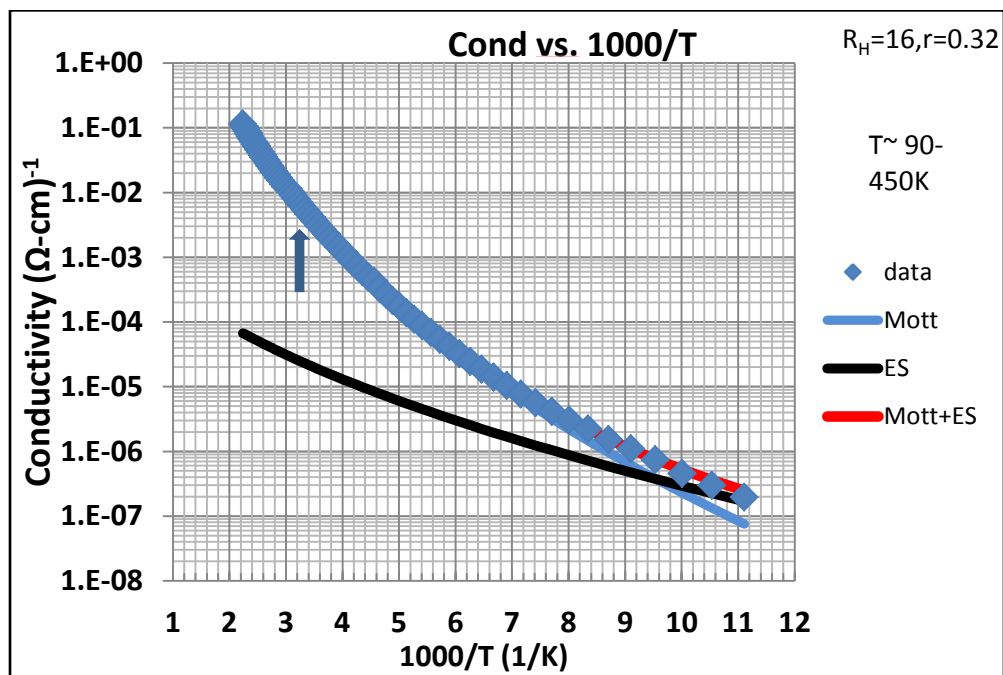


Figure 16. Temperature dependent conductivity for $R_H = 16$, showing the composite of Mott and ES conductivity fits the data.

Table 2. Conductivity prefactors and characteristic temperatures for the Mott and Efros-Shklovskii mechanisms

ID	["r"]	[R _H]	RT resistivity (Ω-cm)	σ _{0M} (Ω-cm) ⁻¹	σ _{0ES} (Ω-cm) ⁻¹	T _{0M} (K)	T _{0ES} (K)
MMC5	0.32	4	103	1.71x10 ¹⁰	0.0011	1.87 x10 ⁸	4360
MMC2	0.32	16	211	3.10 x10 ¹¹	0.0088	3.04 x10 ⁸	10600

In **Figure 17** for the sample with the lowest R_H, the TCR and conductivity are plotted with respect to temperature. It can be seen that for an increase in temperature the conductivity increases and the TCR decreases, as expected. The fitted TCR by the solid line shows that the composite TCR (Eq. 2-30) fits with the numerically obtained values by the derivative of conductivity data.

The numerical derivative provides a more sensitive measure of the contributions to the conductivity than the conductivity alone. Thus, fitting the TCR and the conductivity data assures the most accurate determination of the parameters that best describe the experimental results.

Table 2 shows the related conductivity prefactors and characteristic temperatures for the set of samples having fixed boron doping and R_H = 4 and 16.

It can be seen from the diagrams above that, there is a contribution of both the Mott and the ES to the conductivity, which is represented by the red curve. For the TCR data as well, there is a contribution of the ES at low temperatures and need to account it to add in to the TCR_{Mott} by the formula,

$$|TCR|_{tot} = \frac{\sigma_M}{\sigma_M + \sigma_{ES}} |TCR|_M + \frac{\sigma_{ES}}{\sigma_M + \sigma_{ES}} |TCR|_{ES} \quad \text{Eq. 41}$$

An example of this approach is shown in **Figure 17**, which has wide coverage of temperature on measurement of conductivity.

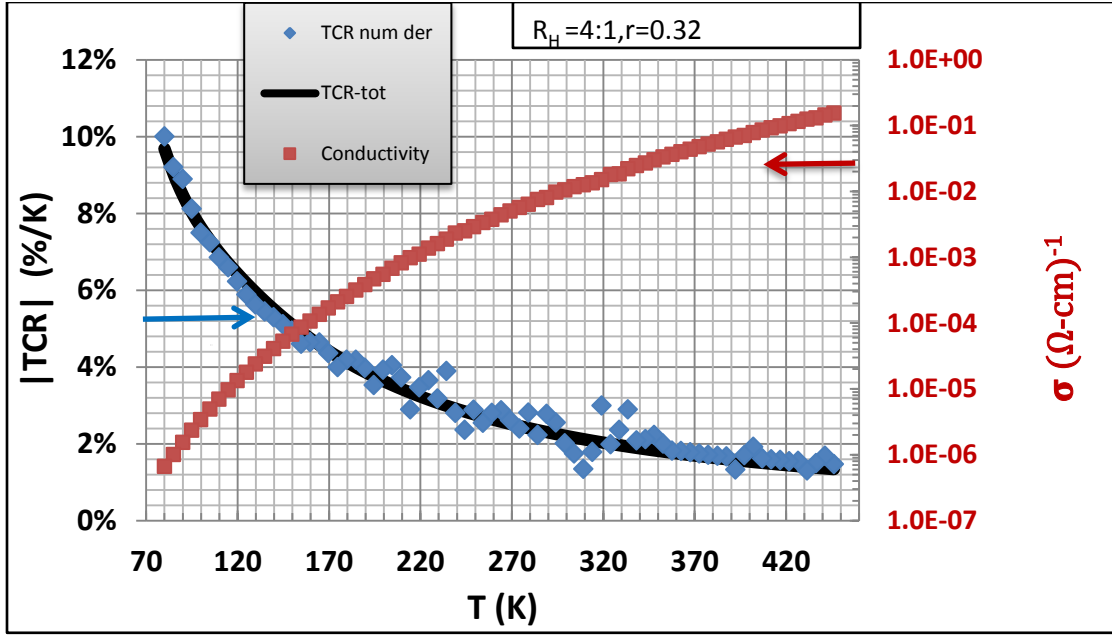


Figure 17. Conductivity and TCR vs. Temperature, showing fit to TCR obtained from experimental conductivity

As indicated in **Figure 17**, the numerically obtained TCR by conductivity data (red squares) and the TCR fit according to the Eq. 41 are in excellent agreement. Hence, the data is best described by combination of the Mott and the ES mechanisms. In the following section, a detail presentation of the several conduction mechanisms associated TCR is presented.

Figure **18** represents the compilation of the TCR results along with the sample having highest H-dilution. The solid lines are the fit according to Eq. 41 to the numerically derived TCR data. The highest dilution sample, $R_H = 100$ solely follows the Mott fit.

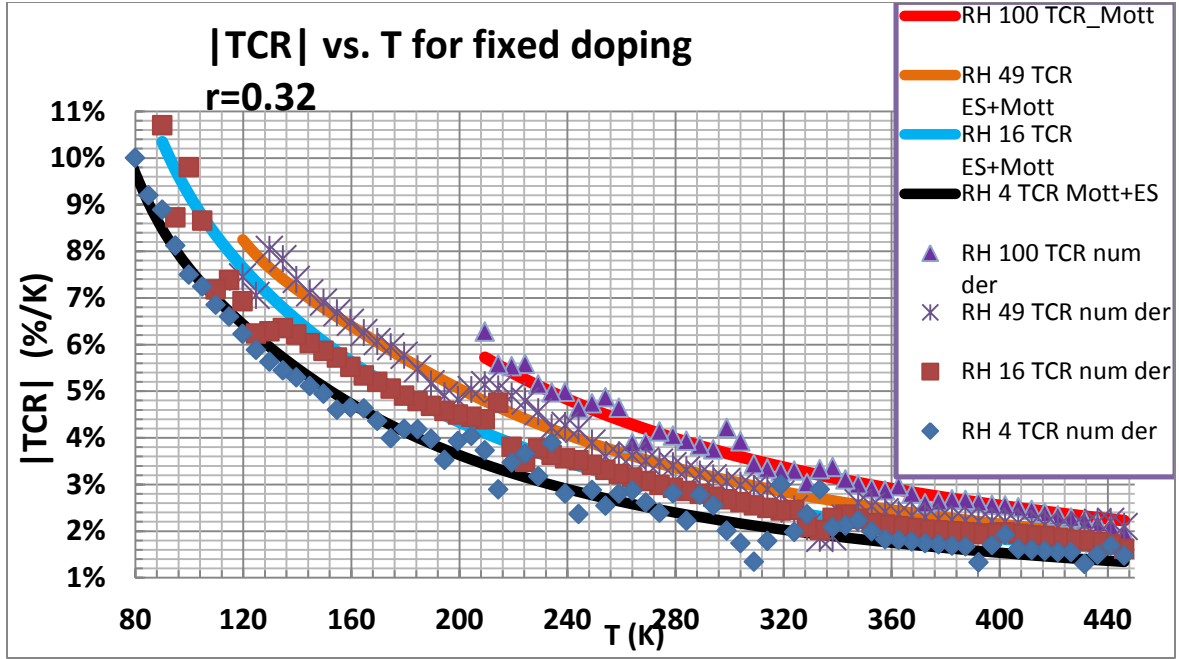
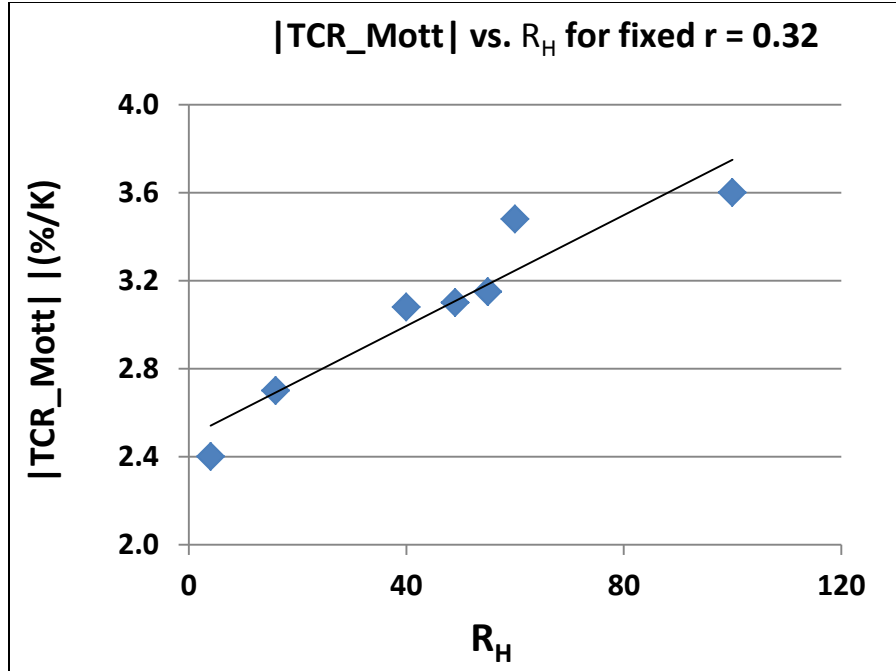


Figure 18. TCR data and the TCR fit for samples having fixed r and varying R_H

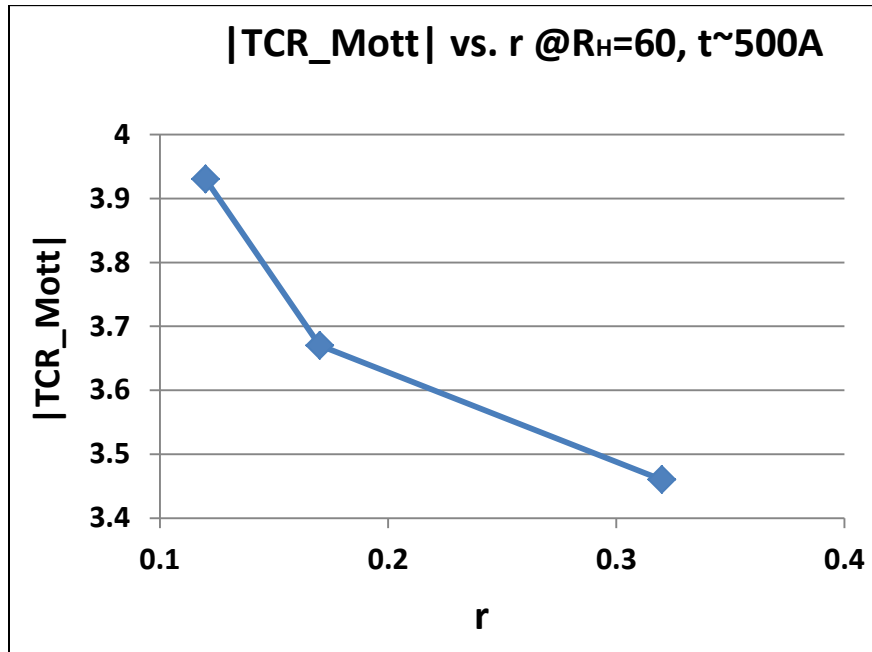
Hence, **Figure 18** shows that the combination of the TCR_Mott and the TCR_ES best describe the TCR data obtained by experiment. The highest dilution sample shown is described by TCR_Mott alone. In addition, it is clear from the figure that, higher value of R_H gives higher TCR, as expected. The Mott parameters are presented in **Table 3** along with the TCR_Mott parameters at room temperature (RT).

The determined parameters are mentioned in the **Table 2** for Mott and Efros parameters. As the conductivity is controlled by different mechanism in different temperature regimes, a comparison of TCR_Mott with TCR_ES using **Eq. 33** and **Eq. 34** can be made. If the T_{oM} (1E8 K) and T_{oES} (1E4 K) values are considered then the ratios of TCR_Mott to TCR_ES is close to 2 at room temperature. It can be concluded that the TCR_ES will be less by a factor of 2 and it will be less compared to TCR_Mott in the range of temperature studied 80-450 K where Mott VRH is the dominant conduction mechanism for the temperature range. Hence, for high TCR, materials with conduction following the Mott mechanism are better than materials with ES mechanism for devices like microbolometers from the performance point of view.

For the fixed boron doping ratio ($r=0.32$) the TCR values at RT are plotted against R_H and boron doping and shown in **Figure 19**.



(a)



(b)

Figure 19. (a) TCR_{Mott} vs. R_H at fixed “ r ” = 0.32 and (b) TCR_{Mott} vs. “ r ” at fixed $R_H = 60$ and different boron doping “ r ” (0.12, 0.17, 0.32)

Figure 19 shows a linear relationship between TCR_Mott and R_H , which is due to the increase of resistivity with the increase of R_H . Additionally, TCR_Mott vs. “r” shows the inverse behavior, as the resistivity decreases with an increase of the boron doping. This implies that there is a competition between boron and silicon to capture hydrogen.

Figure 20 shows the expected increase in the TCR_Mott with an increase of resistivity for fixed “r” and indicates that the TCR linearly increases with an increase in resistivity.

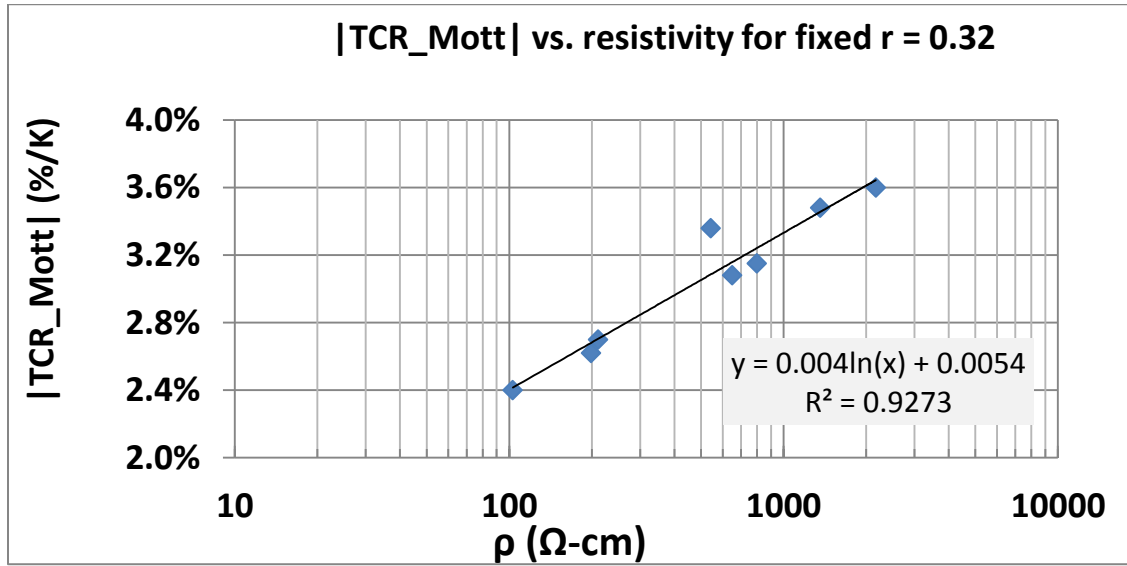


Figure 20. TCR_Mott vs. resistivity for fixed boron doping (highest doping $r = 0.32$ in the family of samples), indicating a trend of increase in TCR as the resistivity increases due to the increase in R_H .

Figure 21 shows the plot for TCR vs. Log ρ for different samples with various doping ratios and dilutions and, as indicated by Eq. 35, shows that TCR is proportional to the log of resistivity.

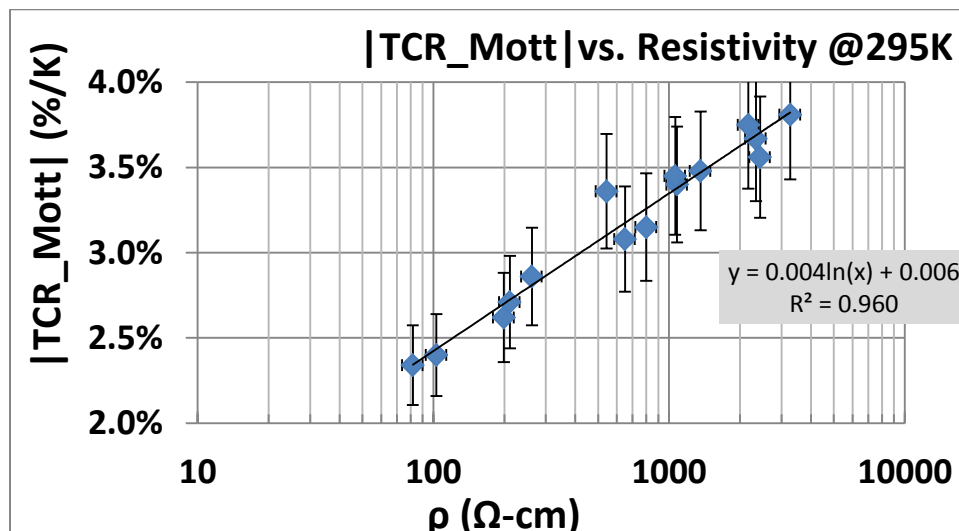


Figure 21. TCR_{Mott} vs. RT resistivity of various samples having different R_H and "r"

From this graph a comparison with the general equation of TCR, (Eq. 35) can be made. Comparing $y = 0.004 \ln(x) + 0.006$ with the equation $TCR = \frac{p}{T} \ln \sigma_0 + \frac{p}{T} \ln \rho$, at room temperature there is a difference by a factor of five between the slope obtained from **Figure 21** with the value of p/T .

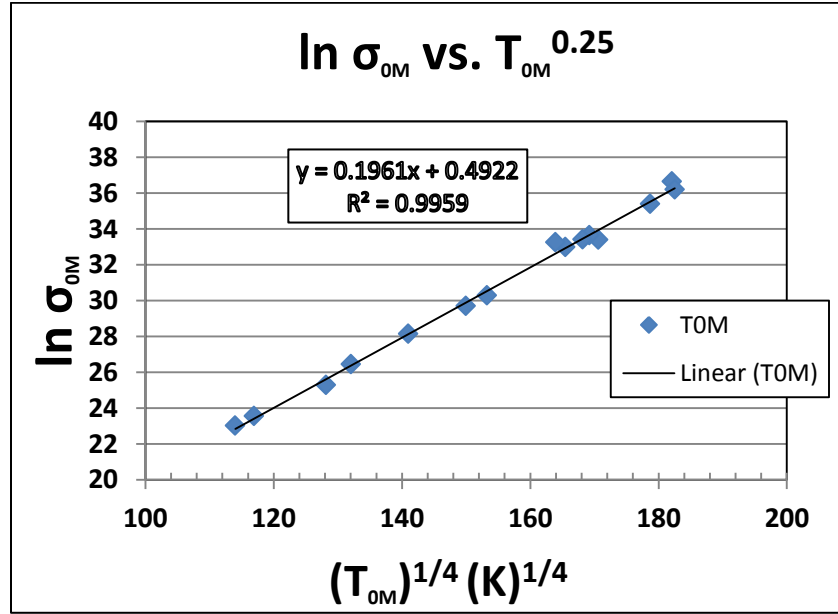


Figure 22. $\ln \sigma_{0M}$ plotted against T_{0M} . The straight line represents the least-squares fit to the data.

The graph of $\ln \sigma_{0M}$ vs. $T_{0M}^{0.25}$, shown in **Figure 22**, gives the equation by experimental data as,

$$\ln \sigma_{0M} = 0.1961 T_{0M}^{0.25} + 0.4922 \quad \text{Eq. 42}$$

As the value σ_{0M} depend on the T_{0M} , the conductivity prefactor will not be a constant. Thus, if the TCR equation is written as,

$$TCR = \frac{p}{T} * \frac{1}{1-AT^p} \{\ln \rho + \ln \sigma_{00}\} \quad \text{Eq. 43}$$

Then at room temperature $T=295$ K, and using the slope of the plot in **Figure 22**,

$$TCR = \frac{0.25}{295(1-0.1961*295^{0.25})} \{\ln \rho + \ln \sigma_{00}\} = 0.0045 \{\ln \rho + \ln \sigma_{00}\} \quad \text{Eq. 44}$$

The graph (**Figure 21**) of TCR vs. ρ gave the equation experimentally as $TCR = 0.0042 \ln \rho + 0.006$. Hence the slope value 0.0042 is in close agreement with the value calculated by the modified equation **Eq. 44**. It can be seen for fixed “r” (for e.g., $r = 0.32$) slopes are close to that shown in **Figure 20**. Recently, Dalvi et al [35] presented an alternate model to describe the conductivity of a variety of disordered materials using a hopping Meyer-Neldel rule. In this case, the quantity “A” in the **Eq. 43** will be equivalent to $(1/T_{MN})^p$ where T_{MN} is the Meyer -Neldel temperature. Thus, although the conductivity follows a M-VRH behavior, the TCR reveals that the conductivity prefactor has a temperature dependence following a variable range hopping Meyer-Nedel rule.

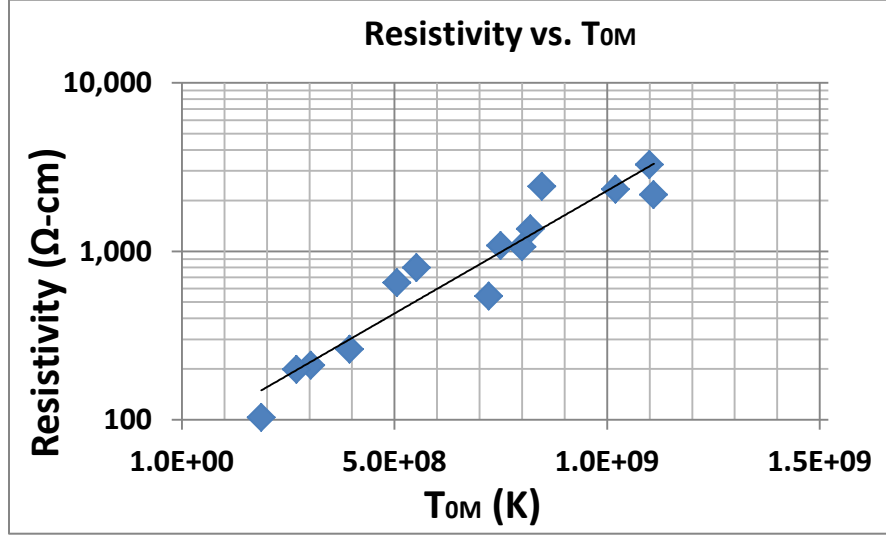


Figure 23. Resistivity vs. T_{0M} at RT of various samples showing an increasing trend of resistivity with the increase of Mott characteristic temperature

Figure 23 shows the Room Temperature dependence of resistivity on the Mott characteristic temperature T_{0M} for different samples varying in R_H at different boron levels, which shows that there is a trend in increase of resistivity with the increase of the Mott characteristic temperature (an analog term similar to activation energy). Further, it can be seen that as the T_{0M} increases both resistivity and TCR increase in similar manner. These values are presented in the **Table 3**.

Table 3. Sample properties - various parameters described in the text.

#	sccm	ID	“r”	R _H	Thick (Å)	Resistivity (Ω-cm)_by IV	TCR_Mott (%/K)	σ _{0-M} 1/ (Ω-cm)	T _{0M} (K)
1	0.7	S140	0.12	60	523	3267	3.81	8.33 x10 ¹⁵	1.10 x10 ⁹
2	1	S063	0.17	55	1092	2433	3.5	3.23 x10 ¹⁴	8.47 x10 ⁸
3	1	S143	0.17	60	521	2336	3.68	2.37 x10 ¹⁵	1.02 x10 ⁹
4	1.9	S150	0.32	100	518	2170	3.75	5.3 x10 ¹⁵	1.11 x10 ⁹
5	1.9	S114	0.32	60	519	1360	3.48	4.10 x10 ¹⁴	8.20 x10 ⁸
6	1	S064	0.17	40	1060	1081	3.4	2.15 x10 ¹⁴	7.50 x10 ⁸
7	1.9	S103	0.32	49	2071	1062	3.45	3.30 x10 ¹⁴	8.00 x10 ⁸
8	1.9	S192	0.32	55	1060	800	3.15	1.45 x10 ¹³	5.52 x10 ⁸
9	1.9	S176	0.32	40	1071	650	3.08	7.99 x10 ¹²	5.06 x10 ⁸
10	1.9	MMG7-B	0.32	49	3270	543	3.1	2.80 x10 ¹⁴	7.22 x10 ⁸
11	1	270A	0.17	10	518	262	2.86	1.70 x10 ¹²	3.95 x10 ⁸
12	1.9	MMC2	0.32	16	3352	211	2.7	3.10 x10 ¹¹	3.04 x10 ⁸
13	1.8	s30	0.3	16	505	199	2.62	9.60 x10 ¹⁰	2.70 x10 ⁸
14	1.9	MMC5	0.32	4	2778	103	2.4	1.71 x10 ¹⁰	1.87 x10 ⁸
15	1.8	2791	0.3	0.1	560	81.8	2.34	1.00 x10 ¹⁰	1.69 x10 ⁸

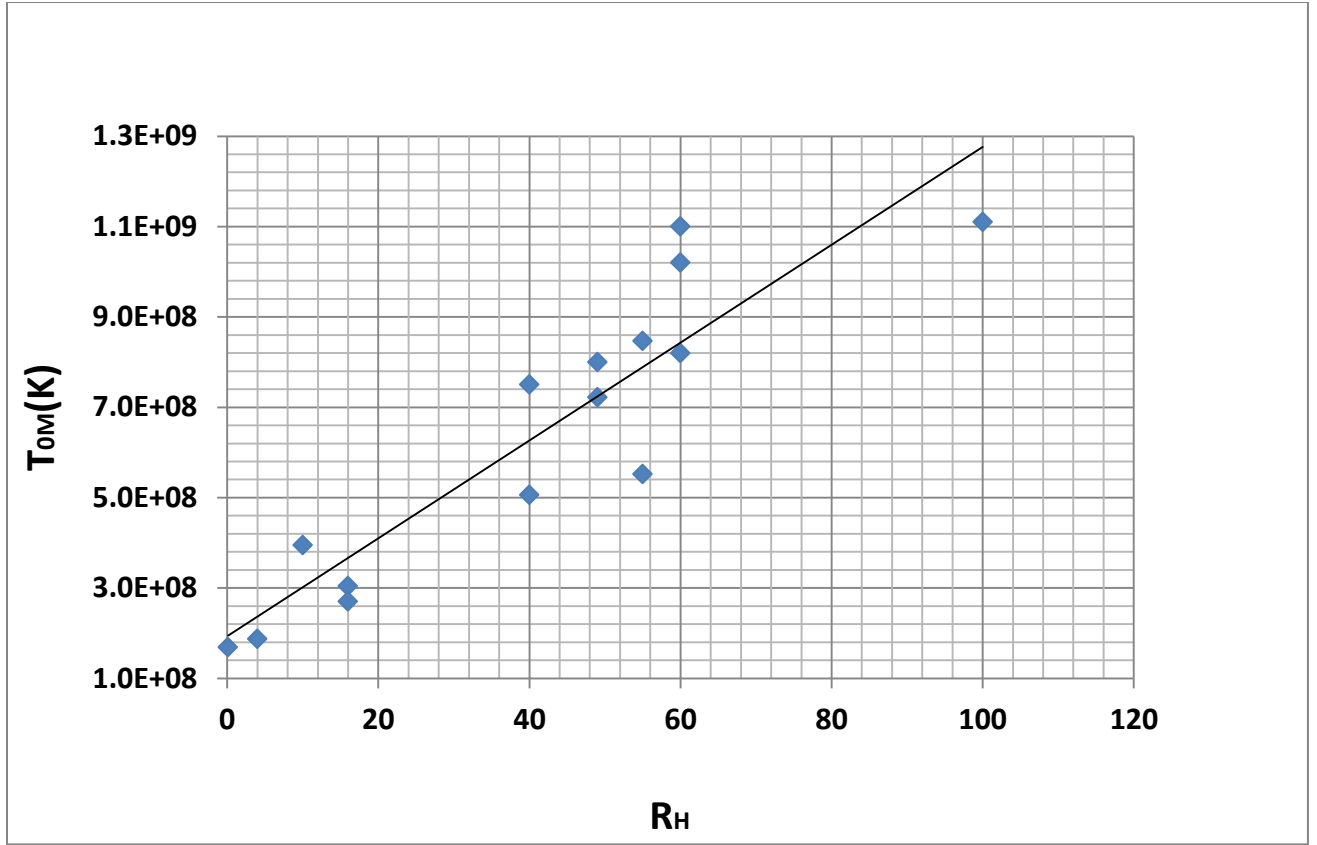


Figure 24. T_{0M} vs. R_H .

The Mott characteristic temperature T_{0M} , which is analogical to the activation energy, shows almost a linear trend with the increase of R_H . The increase of T_{0M} (this depends again on R_H) results in reduction of the conductivity, which is due to the increase of localization length (ξ). This increase is due to the reduction of numbers of traps as a result of better short range order in the a-Si:H matrix. Quantities that correlate with the Mott characteristic temperature are the localization length, hopping distance and energy. The localization length, R_{hop} , and hopping energy can be calculated by using the standard Mott expression. They are given by the wave function localization length,

$$\xi = \left(\frac{18}{K_B T_{0M} N(E_F)} \right)^{1/3} \quad \text{Eq. 45}$$

The hopping distance and hopping energy are, respectively,

$$R_{hop} = \frac{3}{8} \left(\frac{T_{0M}}{T} \right)^{1/4} * \xi \quad \text{Eq. 46}$$

and,
$$W_{hop} = \frac{1}{4} (kT) \left(\frac{T_{0M}}{T} \right)^{1/4} \quad \text{Eq. 47}$$

The values obtained at 300K, assuming a density of state of $1 \times 10^{20} \text{ cm}^{-3} \text{ eV}^{-1}$ is presented in **Table 4**, which summarize the values obtained using Eq. 45 to Eq. 47 for the samples having four different R_H values at fixed boron doping ratio “r”= 0.32.

Table 4. Calculations of wave function localization length, hopping distance and energy at 300K for various R_H values using the Mott characteristic temperature assuming the density of state as indicated.

$N(E_f)$ [1 /cm ³ eV]	Temp	R_H	T_{0M} (K)	loc length (ξ) (Å)	R_{hop} (Å)	$(W)_{hop}$, (meV)	at 300K, R_{hop}/ξ
1×10^{20}	300K	4	1.87×10^8	2.2	23.6	182	10.5
1×10^{20}	300K	16	3.04×10^8	1.9	22.6	205	11.9
1×10^{20}	300K	49	7.22×10^8	1.4	21.0	255	14.8
1×10^{20}	300K	100	1.11×10^9	1.2	20.3	284	16.4

The graphs in **Figure 25** shows that with the increase of R_H , the T_{0M} increases and the localization length decreases. Using Raman measurements, given in section 4.0 these are correlated with the structural configuration of these samples according to the amount of hydrogen. As the structural order improves, there will be less electrically-active defect states, resulting in an increase in the activation temperature and ultimately increases the resistivity and conductivity prefactors.

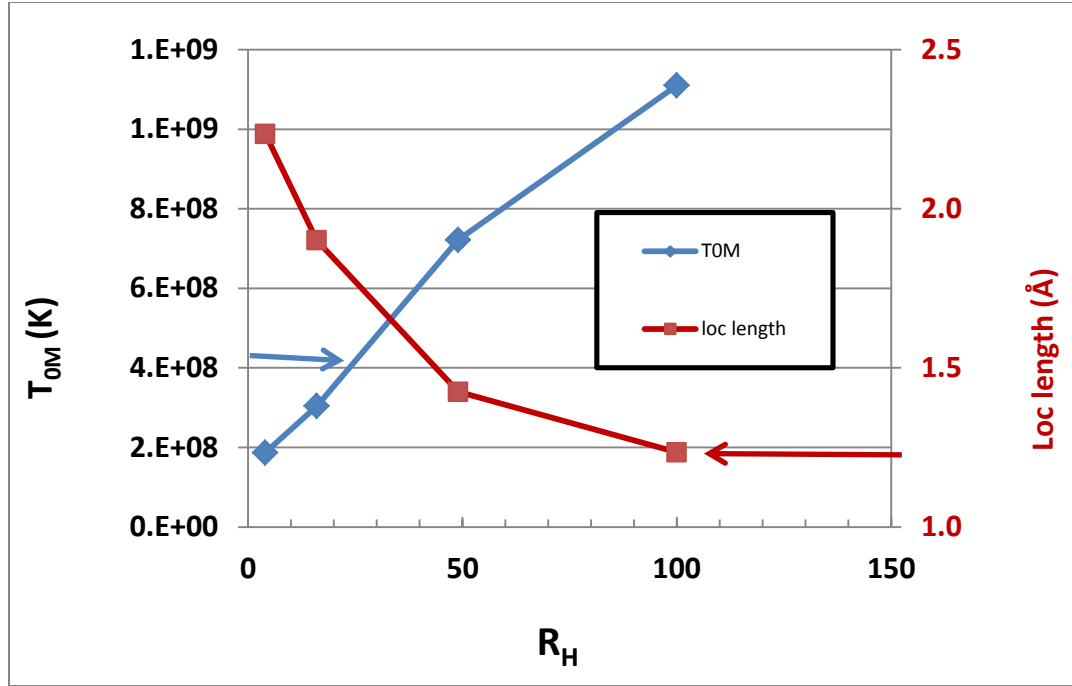


Figure 25. T_{0M} and localization length vs. R_H for the samples having fixed doping ratio “ r ”=0.32

The calculated localization length, hopping distance and hopping energy (W_{hop}) at 300 K, are comparable with values reported by Khan [36] for amorphous silicon nanoparticles prepared by physical vapor condensation method. It is clear from the values presented in the **Table 4** that, the hopping energy increases with the increase of the H-dilution and so does the value “ R_{hop}/ξ ”.

In the same way, the parameters obtained for various boron doping at fixed R_H (60) are presented in **Table 5**.

Table 5. Calculations of wave function localization length, hopping distance and energy at 300K for various boron doping using the Mott characteristic temperature

$N(E_f)$ [1 /cm ³ eV]	Temp	Boron doping “ r ”	T_{0M} (K)	loc length (ξ) (Å)	R_{hop} (Å)	$(W)_{hop}$ (meV)	at 300K, R_{hop}/ξ
1×10^{20}	300K	0.12	1.10×10^9	1.2	20.3	283	16.4
1×10^{20}	300K	0.17	1.02×10^9	1.3	20.4	278	16.1
1×10^{20}	300K	0.32	8.20×10^8	1.4	20.8	263	15.2

Figure 26 shows how the T_{0M} and localization length changes with the change in the boron doping for fixed $R_H = 60$. Since there are more states available due to boron doping, the value of Mott characteristic temperature decreases, and the electrical conduction increases. Accordingly the localization length increases.

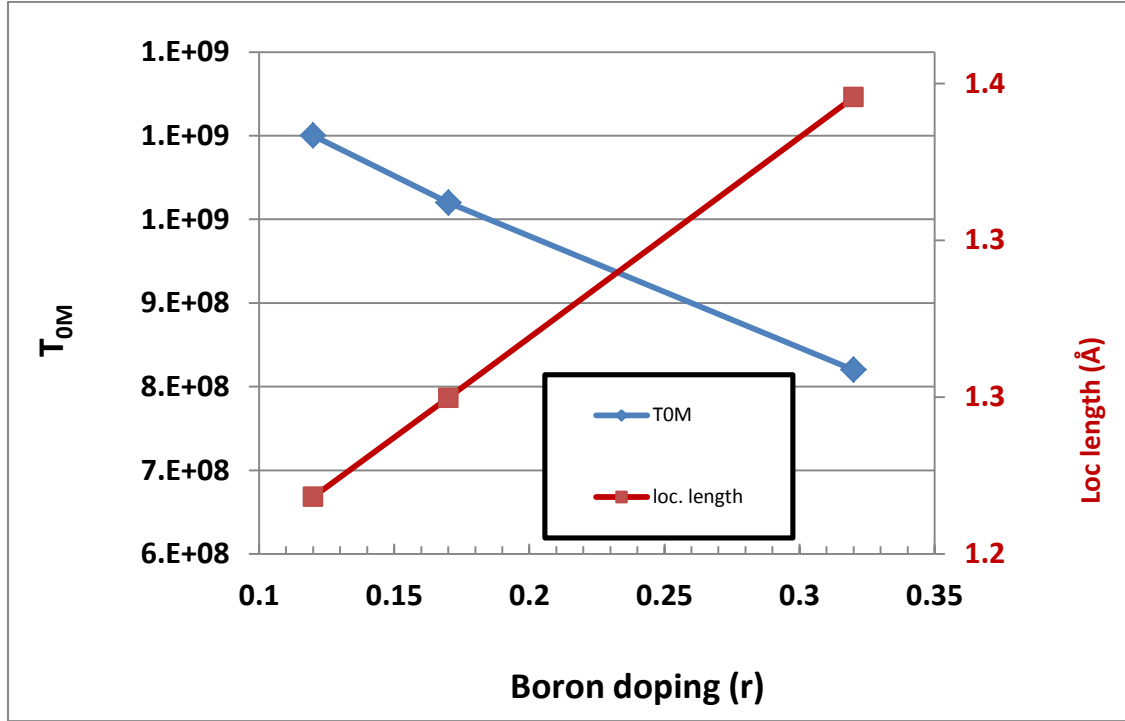


Figure 26. T_{0M} and localization length vs. boron doping for fixed $R_H = 60$.

Unlike in the case of R_H , in this case as the boron doping increases, the Mott parameter (T_{0M}) decreases, whereas the R_{hop} and localization length both increase only slightly. This may be an indication that the effect of hydrogen is strong compared to the boron incorporation. The hopping energy decrease with an increase of boron, as can be seen from the **Table 5** and this is in the opposite direction to the R_H , as indicated by the **Table 4**. Hence, the structural re-arrangement in the a-Si:H matrix due to boron and hydrogen is playing the role in the electrical conduction due to localized states in these samples. This can be understood as a competition of boron and silicon to trap a hydrogen atom, as previously discussed. More about the structural changes will be elaborated on in the Raman section.

The calculations of localization length, hopping distance and the hopping energy by using the T_{0M} value and a nominal value for DOS (Topics in applied physics, Vol. 36, Ed. M. H. Brodsky) of $N(E_F) \sim 1 \times 10^{20} \text{ cm}^{-3} \text{ eV}^{-1}$ for the sample set having (a) fixed boron with different R_H , and (b) fixed R_H with different boron doping levels show that the conditions required for VRH are

fulfilled. These conditions are described by Mott and Davis [8], Yildiz [37], and Khan [36]. The condition for hopping is given as

$$1) W_{hop} \geq k T, 2) \text{ sample thickness } d \gg R_{hop}, \text{ and } 3) R_{hop}/\xi \geq 1.$$

As shown in Table 5 the conditions for the hopping are fulfilled, which indicate that the mechanism is VRH in the material system in the temperature range studied. Also the values obtained for the VRH parameters are close to those found in variety of disordered systems. In addition, H Overhof [38] in his “Mott memorial lecture” reported that the T_{OM} values lie within the range of 1×10^8 K to 1×10^9 K and our values in all the samples are in this range. Therefore, the values obtained in this research for T_{OM} are in excellent agreement with the reported values by different authors. As discussed previously, this parameter is directly linked with the wave function localization length (ξ). Thus **Table 4** shows that, with the increase of R_H , the ξ value decrease and hence decreases of R_{hop} . The wave function is more localized in the traps, making it difficult to hop to other traps, resulting in increase of resistance and hence the resistivity. Of course, this phenomenon depends on temperature, and can be seen in an increase in R_{hop} with a decrease in temperature. The larger value of T_{OM} represents that larger energy is required (in the form of activation temperature, $T_{OM}^{0.25}$) to hop from one site to another for conduction, which make the material more highly resistive. A similar conclusion can be made for boron dependent samples in Table 5 in which the resistivity is less for higher boron doping, due to availability of substitutional sites for hopping due to doping.

3.3. Noise measurements and results

A schematic of the noise measurements is shown in **Figure 27**. The sample is mounted on a copper block within a light tight enclosure. A Keithley 428 source is used to bias the device and is also used as a low noise current amplifier. The gain is adjusted by use of a variable feedback resistor within the preamplifier. The amplified signal is converted to a noise voltage - frequency spectrum by a dynamic signal analyzer (DSA). For these measurements a HP 3562 A was used. The data is then stored on computer for analysis.

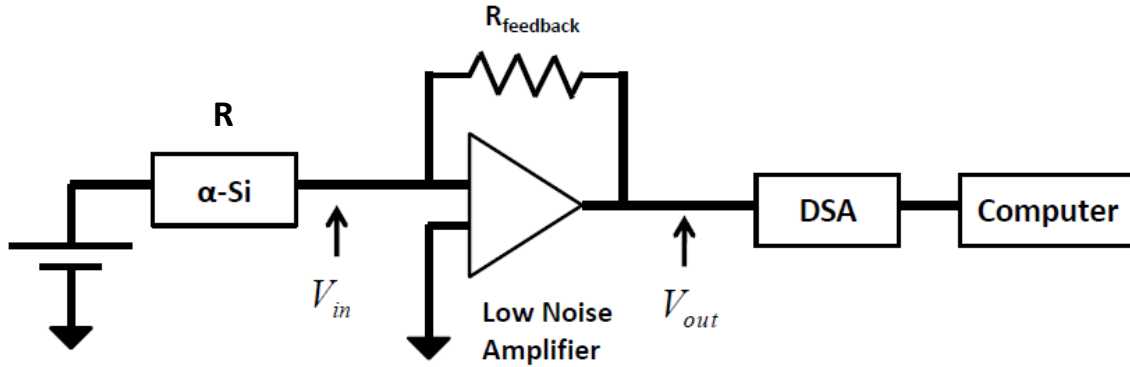


Figure 27. Schematic of apparatus used for noise measurements.

The measured noise, V_m , is

$$V_m^2 = V_{JR_{Fbk}}^2 + (V_n G)^2 \quad \text{Eq. 48}$$

where $V_{JR_{Fbk}}$ is the (Johnson) noise of the amplifier feedback resistor, V_n is the sample noise and G is the amplifier gain. The gain is the ratio of the amplifier output signal voltage, V_{out} , to the input signal voltage, V_{in} , which is equal to the ratio of the feedback resistance to the sample resistance, R .

$$G = \frac{V_{out}}{V_{in}} = \frac{R_{Fbk}}{R} \quad \text{Eq. 49}$$

The amplifier gain is usually set in the range $G = 1 - 10$ by appropriate selection of the feedback resistance. The system noise is also characterized by using low noise metal film resistors whose

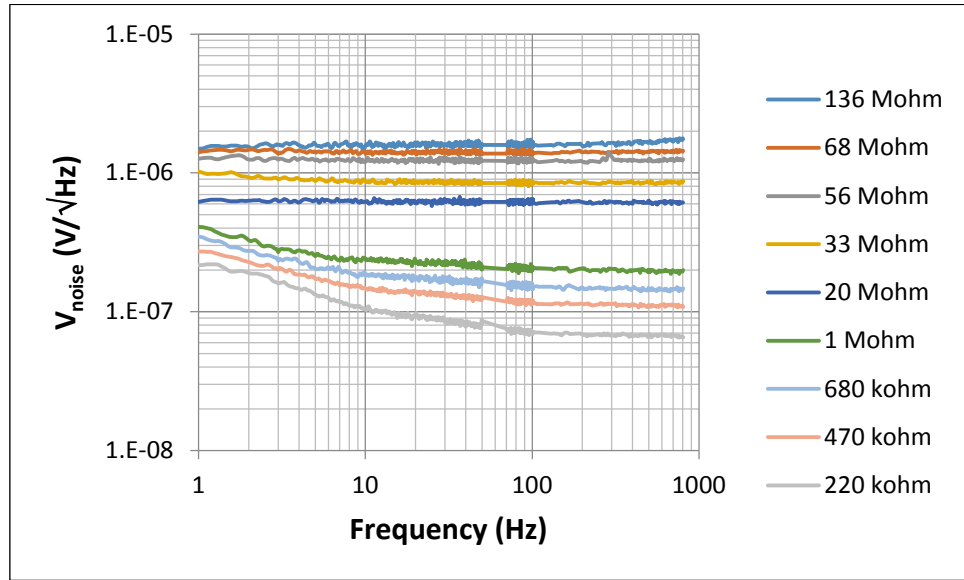


Figure 28. Noise measurements made on metal film resistors with resistances ranging from 220 kΩ to 136 MΩ.

resistances are comparable to the devices tested. As shown in **Figure 28**, for our system, for metal film resistors $R_{MF} > 20 \text{ M}\Omega$, the system noise voltage does not depend on frequency (1 to 1000 Hz). For $R_{MF} < 20 \text{ M}\Omega$, and $f < 10 \text{ Hz}$, the system noise voltage depends on frequency. As the resistance decreases, this effect is more pronounced.

The temperature dependence of low frequency noise was measured on a-Si:H films grown by plasma enhanced chemical vapor deposition (PECVD) at differing boron dopant source concentration, r , and hydrogen dilution, R_H , of the silane precursor.

The total noise measured is comprised of $1/f$ noise, white noise, and potentially G-R noise, which can be expressed quantitatively as,

$$\frac{V_{noise}^2}{\Delta f} = \frac{V_{1/f}^2}{\Delta f} + \frac{V_{white}^2}{\Delta f} + \frac{V_{G-R}^2}{\Delta f} \quad \text{Eq. 50}$$

The 1/f noise can be described using the Hooge model [39], with

$$\frac{V_{1/f}^2}{\Delta f} = \frac{\alpha_H}{P} \frac{V_{Bias}^2}{f^\gamma} = \frac{\alpha_H}{pV} \frac{V_{Bias}^2}{f^\gamma} = \frac{B}{f^\gamma} \quad \text{Eq. 51}$$

where P is the total number of carriers, p is the carrier density, V is the device volume, V_{Bias} is the device bias, and γ is the frequency exponent, typically near a value of 1 (in the range from 0.9 to 1.1) [39]. The normalized Hooge parameter is α_H/p , where α_H is the Hooge coefficient. For the Hooge model,

$$\sqrt{B} = \sqrt{\frac{\alpha_H}{pAt}} V_{Bias} \quad \text{Eq. 52}$$

or

$$B = \left(\frac{\alpha_H}{pt} V_{Bias}^2 \right) \frac{1}{A} \quad \text{Eq. 53}$$

where A is the device area, and t is the film thickness. As a result, $\sqrt{B} \sim V_{bias}$ and $B/V_{bias} \sim 1/A$ for fixed bias voltages.

The Generation-Recombination (G-R) noise for a single trap is described by [40,41]

$$\frac{V_{G-R}^2}{\Delta f} = \frac{A_t \tau V_{Bias}^2}{1 + (2\pi f \tau)^2} \quad \text{Eq. 54}$$

where τ is the trap time constant and $A = \frac{n_t}{Vn^2}$. Here, n_t is the trap density, V is the device volume, and n is the carrier density. The noise waveform can be analyzed for trapping by subtracting the white noise from the measured noise, normalizing this difference with the square of the bias voltage, and multiplying by the frequency, where

$$f \frac{(V_{noise}^2 - V_{white}^2)}{V_{Bias}^2} = \frac{\alpha_H}{P} + \frac{fA_t \tau}{1 + (2\pi f \tau)^2} \quad \text{Eq. 55}$$

Here it is assumed that the exponent γ of the $1/f$ noise frequency is equal to 1. For the case of a single trap, a plot of the left side of **Eq. 55** (determined from the measured noise data) yields a horizontal line (of value α_H/p) superimposed with a Lorentzian (trap).

Figure 29 shows the low frequency noise as a function of temperature. The Very Low Frequency Noise (V_{LFN}) is defined as the device noise at 1 Hz at a bias voltage of 1 V. V_{LFN} appears to have little or a slight temperature dependence for temperatures between 200 and 380 K. However, for temperatures greater than 400 K, the low frequency noise increases significantly with increasing temperature. This data suggests that there are different noise contributions for these two temperature ranges. **Figure 29 (b)** shows the low frequency exponent γ as a function of temperature. The exponents were determined by a power fit to the device noise data. The frequency exponent is typically between 0.9 and 1.1 for temperatures less than 400 K, indicative of $1/f$ noise. For temperatures greater than 400 K, the exponent is greater

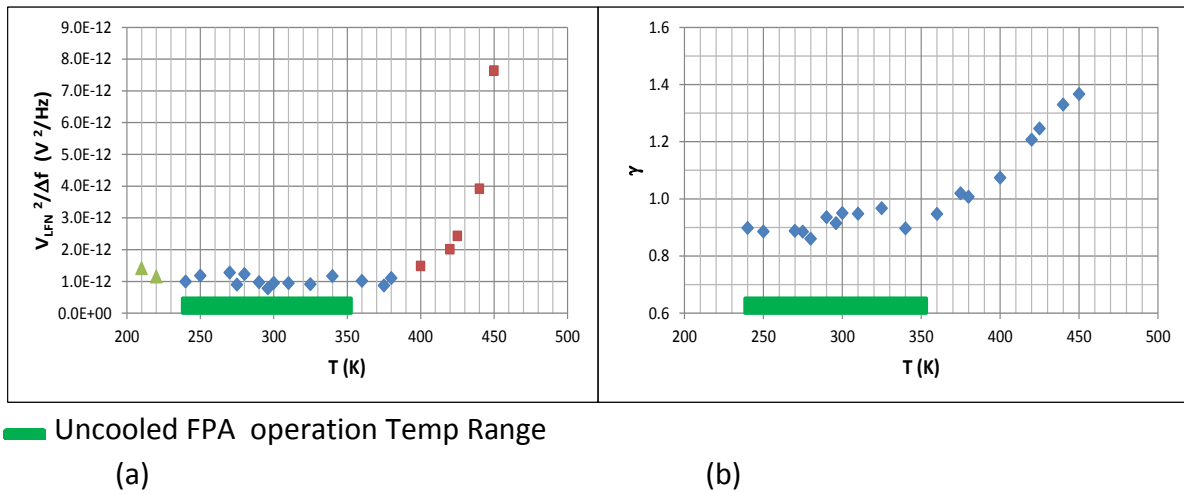


Figure 29. (a) The low frequency noise as a function of temperature, and (b) the frequency exponent as a function of temperature.

than 1 and is indicative that the device low frequency noise is comprised of more than $1/f$ noise.

Therefore, in the uncooled FPA operating temperature range $[-40^\circ\text{C}$ to $80^\circ\text{C}]$ the Low Frequency Noise is $1/f$ and is nearly independent of temperature.

For temperatures above 400 K, the low frequency noise increases more rapidly with increasing temperature and the frequency exponent γ is significantly larger than 1. As a result, the noise waveforms were analyzed for trapping using **Eq. 55**. **Figure 30** shows $f(V_{noise}^2 - V_{white}^2)/V_{Bias}^2$ as a function of frequency for temperatures of 360 K, 380 K, 400 K, 420 K, and 440 K. For temperatures of 360 K and 380 K, the curves have no slope, indicative that the measured low frequency noise is $1/f$ noise only. The values of these curves are equal to α_H/p . For temperatures 400 K and above, the curves at low frequency increase with increasing temperature.

This phenomenon is characteristic of a trap contributing to the total noise voltage. It is believed that this is due to a deep trap in a-Si:H.

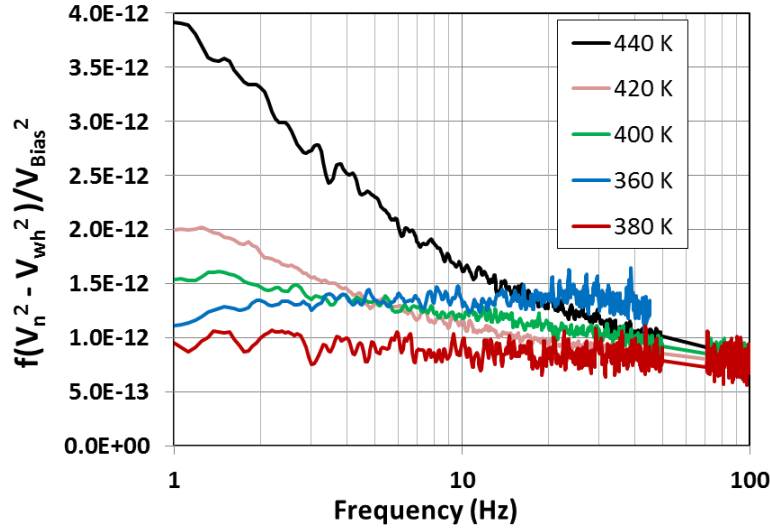


Figure 30. Noise waveforms were analyzed for trapping at temperatures of 360 K, 380 K, 400 K, 420 K, and 440 K.

Figure 31 shows α_H/p determined from the noise data as a function of Mott temperature. The $1/f$ noise was measured at Room Temperature and the Mott characteristic temperature T_{0M} was obtained from temperature dependent conductivity measurements. The normalized Hooge parameter α_H/p is observed to increase with Mott temperature with an exponential trendline in qualitative agreement with theory [29,30]. For a specific temperature the Hooge parameter α_H/p is determined from the value of T_{0M} .

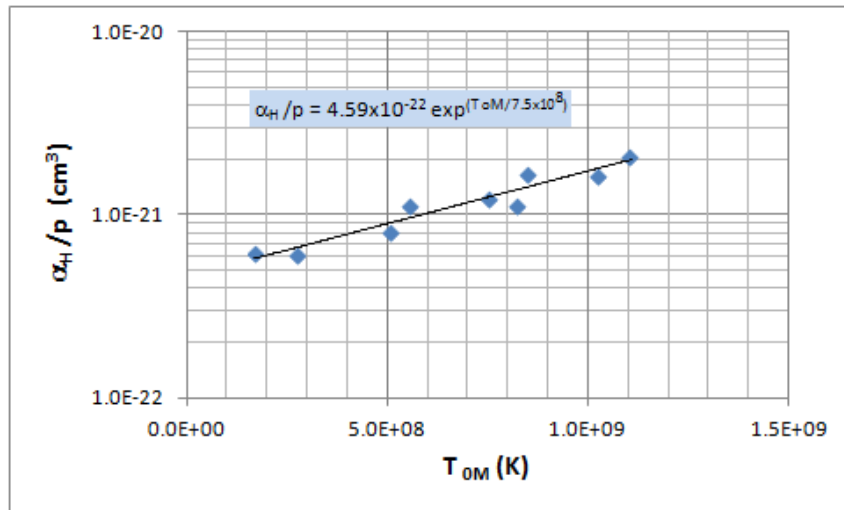


Figure 31. α_H/p as a function of Mott temperature.

TCR and noise correlation

As described in Section 3.2, TCR in p-type a-Si:H, grown with a specific boron dopant precursor, depends linearly on T_{0M} according to Eq. 33, i.e., $TCR \approx T_{0M}^{1/4}$. We also found that 1/f noise is related to T_{0M} , in a nearly exponential dependence, $\alpha_H/p \approx \exp[T_{0M}]$, as shown in **Figure 31**. This suggests that TCR and 1/f noise are correlated via the Mott characteristic temperature T_{0M} . Shown in **Figure 32** is a plot of the normalized Hooe parameter vs.TCR at room temperature following an exponential trend.

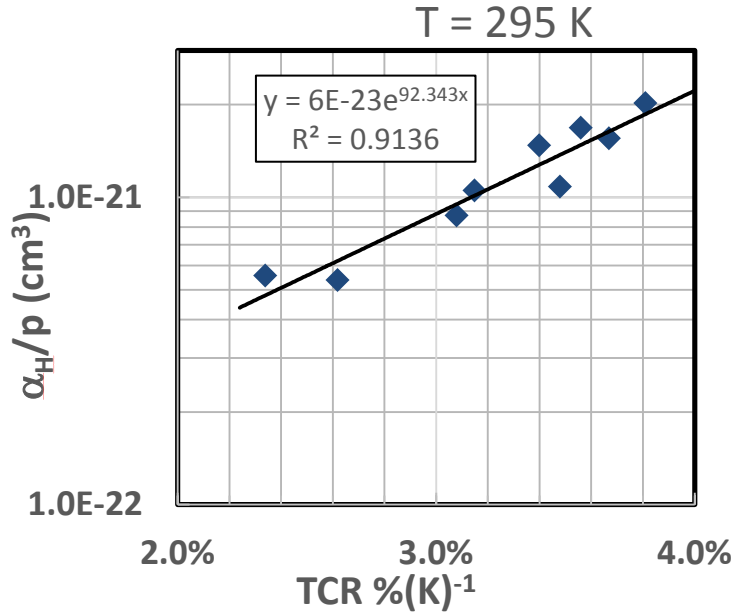


Figure 32. The normalized Hooe parameter α_H/p as a function of TCR for BCl₃-doped p-type a-Si:H.

4.0 Optical Characterization

4.1 Raman Measurements and Results

Raman spectroscopy is one of the most widely used techniques to understand the local crystal structure of amorphous materials since it provides information about the bonding network order in such materials. It is a nondestructive measurement which provides information about the short range order (SRO) and mid-range order (MRO) [42,43,44]. The SRO of an amorphous material is usually associated with the nearest neighbor coordination [45] and the MRO involves the topology of the network at the level of third or fourth nearest neighbor and described by the size and distribution of rings of constituent atoms [46]. Various groups have used Raman spectroscopy to study the changes in the local crystal structure of a-Si:H by investigating the changes in the transverse optical (TO) and transverse acoustic (TA) modes of vibration [46,47,48]. These studies show that the intensity ratio of the TA and TO modes (I_{TA}/I_{TO}), full width half maximum of the TO mode (Γ_{TO}), and the central wavenumber (ω_{TO}) of the TO modes depend on growth method, growth temperature, and hydrogen content. In plasma enhanced chemical vapor deposition (PECVD) growth, the structural configuration of a-Si depends on the H-dilution of the silane precursor and the thickness of the thin film, and can yield different states such as amorphous, nano/micro crystalline and polycrystalline phases [6,49]. In addition, structural changes in a-Si:H films due to hydrogen incorporation and doping have been reported [50,51,52,53]. The addition of boron results in local structural changes resulting from the formation of chemical bonds, such as B-Si and B-H-Si [54], results in an increase in bond angle and bond length, leading to a degradation of the SRO. Specifically, it has been shown that hydrogen diluted crystallization is mediated by insertion of H atoms into Si-Si bonds through the formation of a Si-H-Si bonding configuration when H atoms diffuse in a-Si:H matrix, resulting in improved crystallinity, i.e., improvement in SRO [54]. Infrared spectroscopic results [53,55] have shown that, with the addition of boron, there is a competition between boron and silicon to form bonds with the hydrogen, resulting in an increase in B-H stretching mode bonds and a decrease in Si-H bonds as the boron concentration is increased.

In preliminary work by our group [56], it was observed that an increase of Boron doping broadens Γ_{TO} , indicating retardation in the formation of microcrystals in the film, resulting in an increase in structural disorder. It was also shown that higher growth temperature and higher H-dilution promotes improvement in the atomic order of boron-doped a-Si:H films grown by PECVD.

In this report, room temperature Raman spectra from boron doped p-type a-Si:H thin films prepared by PECVD at two growth temperatures for various levels of H-dilution and boron

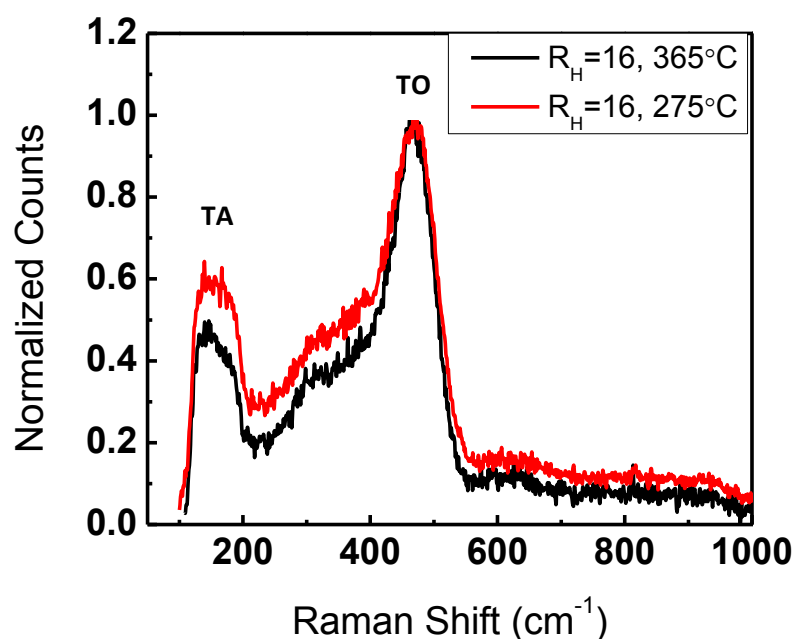
doping are presented, and the effect of these parameters on the phonon modes of vibration are discussed. It is found that there is a strong relationship between the local structural order and the growth parameters of temperature, H-dilution and boron doping. The results show that, with either an increase of H-dilution or with increased growth temperature, the SRO and MRO of the a-Si:H films improve, as evidenced by a decrease of both Γ_{TO} and the intensity ratio (I_{TA}/I_{TO}) of the TA and TO vibrational modes [57]. In addition, the effect of H-dilution on SRO and MRO decreases at increased sample growth temperature and, for samples with fixed H-dilution, an increase in boron doping results in a decrease in the SRO. Finally, the electrical resistivity of the samples prepared at the higher growth temperature correlates with Γ_{TO} and ω_{TO} , where the resistivity increases with decreasing Γ_{TO} , and increasing ω_{TO} results from the improvement in SRO.

Experimental

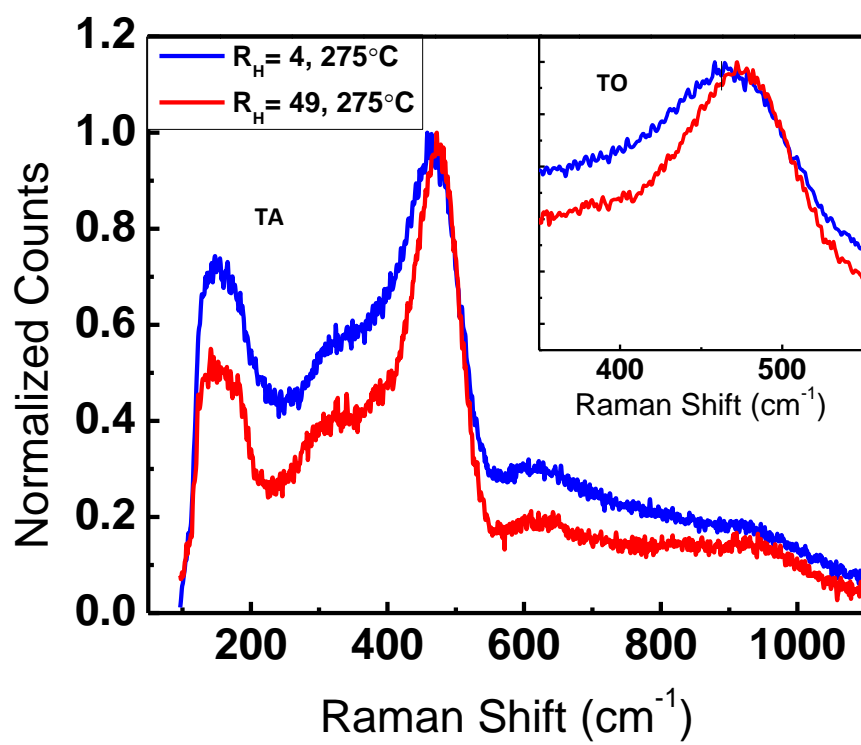
Several a-Si:H thin films were grown by PECVD at the substrate temperatures of 275°C and 365 °C. The thickness of the films investigated ranged from approximately 1000 Å to 3000 Å. The flow rate ratio of boron to silane, defined as “r” = $[BCl_3]/[SiH_4]$, and H-dilution to silane ratio “ R_H ” = $[H_2]/[SiH_4]$, were varied to produce films with differing hydrogen and boron concentrations. The samples reported here were grown at R_H values ranging from 4 to 55 and with “r” values of 0.17 and 0.32. A Thermo Electron Almega XR Raman Spectrometer with a 532 nm laser as an excitation source and a 2.5 micron spot size was used to obtain room temperature Raman spectra.

Results and Discussion

The Raman spectra for different growth temperatures and H-dilutions for a fixed flow rate ratio of boron $r = 0.32$ are shown in the **Figure 33**. In agreement with the growth phase diagram [6], increasing H-dilution for a fixed boron doping and growth temperature results in a decrease in Γ_{TO} , indicating better structural order with an increase of H-dilution. Specifically, **Figure 33 (a)** shows spectra obtained for a fixed H-dilution of $R_H = 16$ for films grown at 275 °C and 365 °C. It is clearly seen that when either R_H , growth temperature, or both increase, Γ_{TO} narrows, indicating an improvement in SRO. In addition, the intensity ratio, I_{TA}/I_{TO} , decreases, indicating an improvement in the MRO. The spectra shown in **Figure 33 (b)** better illustrates the effects of H-dilution on the improvement in local structural order. At the lower growth temperature, an increase in hydrogen concentration results in a substantial improvement in the local structure (i.e., SRO and MRO), as evidenced by a decrease of both Γ_{TO} and the intensity ratio (I_{TA}/I_{TO}) of the TA and TO vibrational modes. This improvement in local order is further supported by the spectra shown in the inset, which shows that, at higher H-dilutions, the TO peak shifts to higher wavenumber.



(a)



(b)

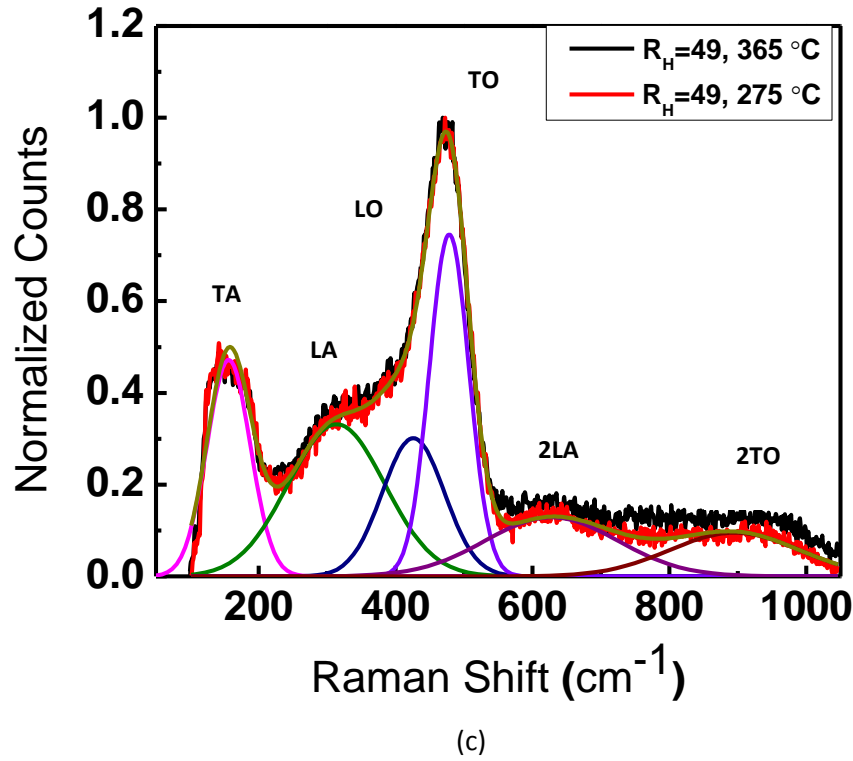
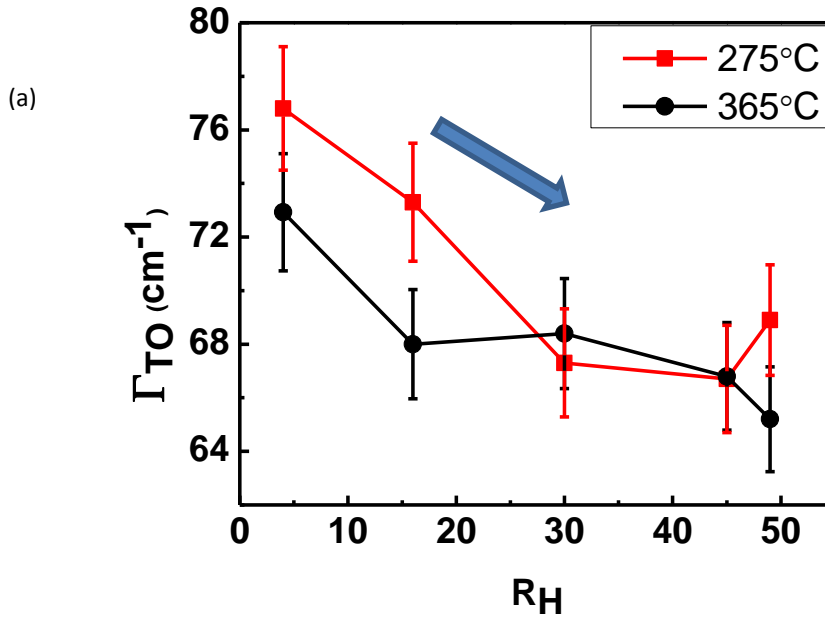


Figure 33. Representative Raman spectra for the doping level $r = 0.32$ (a) for a fixed H-dilution at growth temperatures 275 °C and 365 °C (b) for the H-dilutions of $R_H = 4$ and 49 at a growth temperature of 275 °C and (c) For the H-dilution ($R_H = 49$) at growth temperatures 275 °C and 365 °C, showing deconvoluted Raman peaks from left to right: TA ($\omega = 155.5 \text{ cm}^{-1}$), LA ($\omega = 312.1 \text{ cm}^{-1}$), LO ($\omega = 425.5 \text{ cm}^{-1}$), TO ($\omega = 477.8 \text{ cm}^{-1}$), 2LA ($\omega = 625.6 \text{ cm}^{-1}$), and 2TO ($\omega = 895.8 \text{ cm}^{-1}$).

Figure 33 (c) illustrates effect of growth temperature on the ability of hydrogen to improve the short- and mid-range order of the a-Si:H thin film. This figure shows spectra obtained for the highest H-dilution of $R_H = 49$ for films grown at 275 °C and 365 °C. At this high H-dilution the Raman spectra obtained at both growth temperatures are virtually identical. This can be understood in terms of changes in the amorphous structure due to bonding nature of silicon with hydrogen. Higher H-dilution affects the growth structure as the kinetics of atom incorporation changes by changing the constituent elements by the formation of either Si-H or Si-H₂. It has been shown by *ab initio* calculations that mobile hydrogen atoms break strained silicon bonds to form Si-H and Si-H₂ [58]. From the infrared spectroscopy it has been reported that, with the increase of H-dilution, silicon monohydride absorption peaks increase in strength whereas silicon dihydride absorption peaks decrease [54]. For fixed doping and dilution, the silicon monohydride absorption peak is significantly larger for lower growth temperature, as shown in section 4.2, which can be attributed to additional hydrogen atoms being absorbed. On the other hand, the higher growth temperature adds surface mobility to the absorbed reactant species, which increases the likelihood of lower energy bond configurations. Further, the higher growth

temperature increases the desorption or dissociation of weakly bonded species, reducing the net deposition rate and increasing the likelihood that stronger bond configurations are prevalent. Thus, the improvement in SRO and MRO at each growth temperature due to the formation of Si-H and Si-H₂ bonds overcomes any action of the higher growth temperature to decrease the absorption of hydrogen. It has been shown in glow discharge grown undoped a-Si:H that mechanical stress is not primary factor for the change of central frequency position of the TO mode [59]. As a result, it is concluded that the improvement in the local order results primarily from the increase in H-dilution.

As previously discussed, growth temperature and H-dilution causes significant changes in the structural order of a-Si:H thin films. To better quantify the observations shown in **Figure 33 (c)**, Gaussian deconvolution was performed on each spectrum, using 6 Gaussian peaks representing the TA, LA, LO, TO phonon modes and replica peaks of the LA and TO phonon modes, respectively. The results are shown in **Figure 34**. **Table 6** shows the Raman parameters measured for various samples.



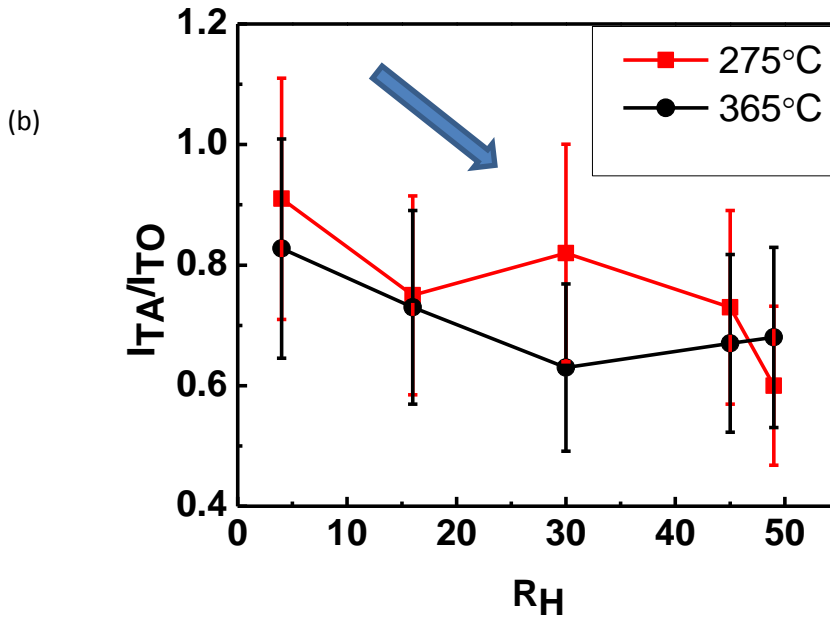


Figure 34. (a) Γ_{TO} vs. H-dilution, indicating improvement in SRO with increase of H-dilution for “ r ”=0.32 (b) intensity ratio (I_{TA}/I_{TO}) vs. H-dilution indicating improvement in MRO with increase of H-dilution for “ r ”=0.32

Figure 34 (a) shows Γ_{TO} plotted with respect to the H-dilution ratio (R_H) for both growth temperatures. As the H-dilution is increased, Γ_{TO} decreases, indicating improvement in the SRO. It can be seen from **Figure 34 (a)** that, the effect of growth temperature on structural order decreases with increasing H-dilution. **Figure 34 (b)** shows a gradual decrease in the intensity ratio I_{TA}/I_{TO} with an increase of H-dilution, indicating a trend of gradual improvement in the MRO. It can be speculated that the topology of the network improves with the increase of H-dilution [10].

Figure 35 shows the influence of boron doping on the SRO, illustrated for two H-dilutions ($R_H = 40$ and 55) and two different boron doping levels ($r = 0.17$ and 0.32)

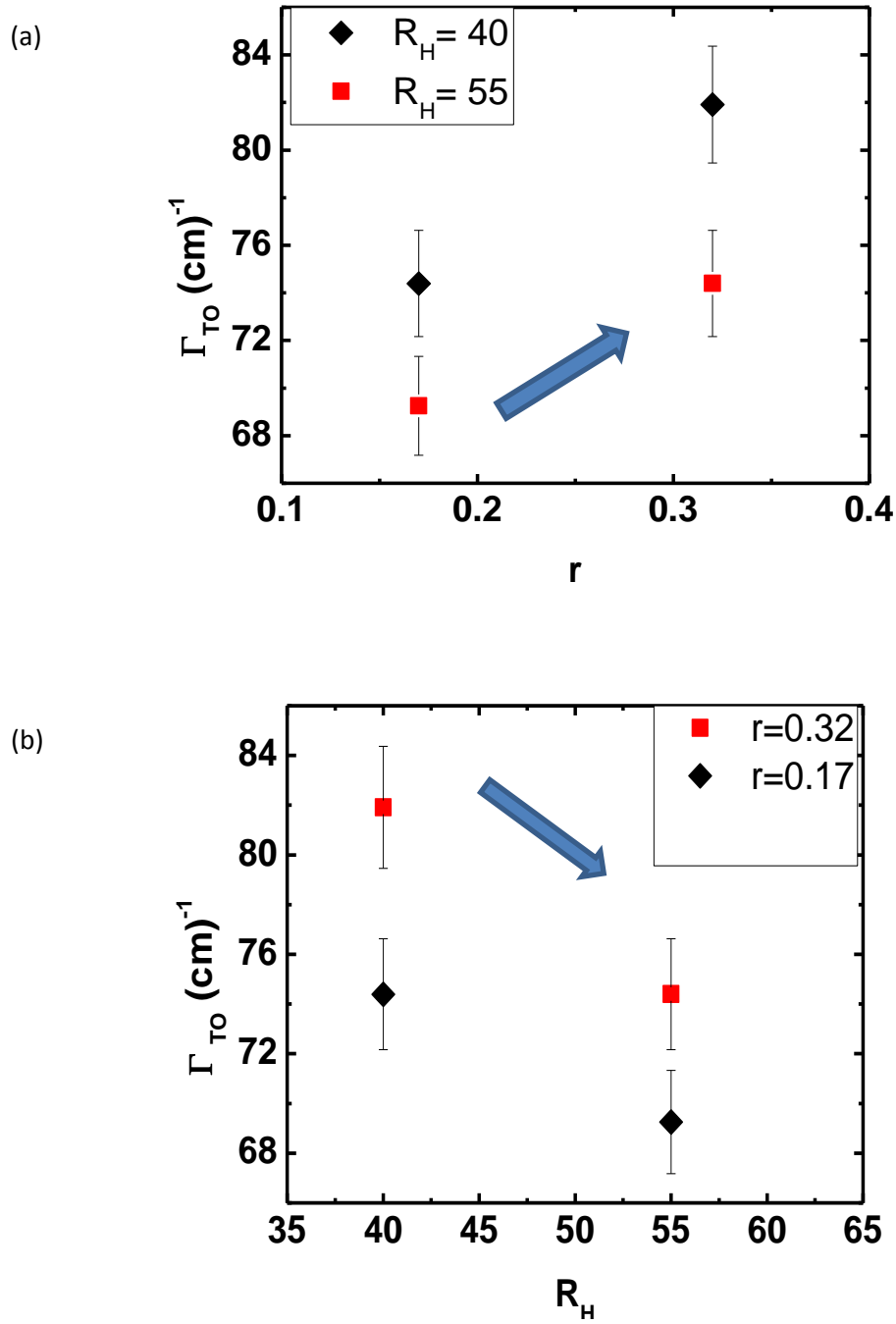


Figure 35. (a) Γ_{TO} vs. boron incorporation, “ r ”, and (b) Γ_{TO} vs. H-dilution, R_H .

As is seen in **Figure 35 (a)** for both H-dilutions shown, Γ_{TO} increases with increasing boron concentration, indicating degradation in SRO. Illustrated differently, as shown in **Figure 35 (b)**, Γ_{TO} decreases with increasing H-dilution for each boron concentration, indicating that an increase in hydrogen concentration overcomes the effects of boron on the SRO. This suggests

that there is a competition between boron and silicon to capture a hydrogen atom and that the degradation in SRO results from a rearrangement of chemical bonding in a-Si:H.

Table 6. Raman parameters (TO frequency, TO line width and intensity ratio I_{TA}/I_{TO}) for measured a-Si:H thin film samples.

Growth Temperature (°C)	Thickness (Å)	Boron doping [BCl ₃]/[SiH ₄]	H-dilution [H ₂]/[SiH ₄]	ω_{TO} (cm) ⁻¹	Γ_{TO} (cm) ⁻¹	I_{TA}/I_{TO}
365	2778	0.32	4	473.1±1.9	72.9±2.6	0.83±0.17
365	3199	0.32	16	474.1±1.9	68±2.4	0.73±0.15
365	3199	0.32	30	477.5±1.9	68.4±2.4	0.63±0.13
365	3162	0.32	45	475.2±1.9	66.8±2.3	0.67±0.13
365	2986	0.32	49	477.2±1.9	65.2±2.3	0.68±0.14
275	3000	0.32	4	473.8±1.9	76.8±2.7	0.91±0.18
275	3000	0.32	16	473.8±1.9	73.3±2.6	0.75±0.15
275	3000	0.32	30	477.0±1.9	67.3±2.4	0.82±0.16
275	3000	0.32	45	475.3±1.9	66.7±2.3	0.73±0.15
275	3000	0.32	49	477.8±1.9	68.9±2.4	0.6±0.12
365	1060	0.32	55	472.0±1.7	74.4±2.2	0.34±0.02
365	1071	0.32	40	471.9±1.7	81.9±2.5	0.44±0.03
365	1092	0.17	55	479.0±1.7	69.3±2.1	0.52±0.04
365	1060	0.17	40	476.5±1.7	74.4±2.2	0.48±0.03

The Raman results show that the structural properties depend strongly on growth temperature and the plasma chemistry. It is well known that hydrogen passivates the dangling bonds of a-Si [10]. However as seen from **Figure 33 (c)**, increasing the hydrogen supply in the plasma at the higher growth temperature has little effect on the Raman spectra. This indicates that the growth kinetics of PECVD a-Si:H favor hydrogen incorporation into the a-Si thin film at lower growth temperatures. The results presented here agree with and extend those obtained at lower temperatures [57] which showed that the development of the local structure (SRO and MRO) in a-Si:H depends on the initial ordering of the amorphous network which, in turn, is determined by the growth temperature.

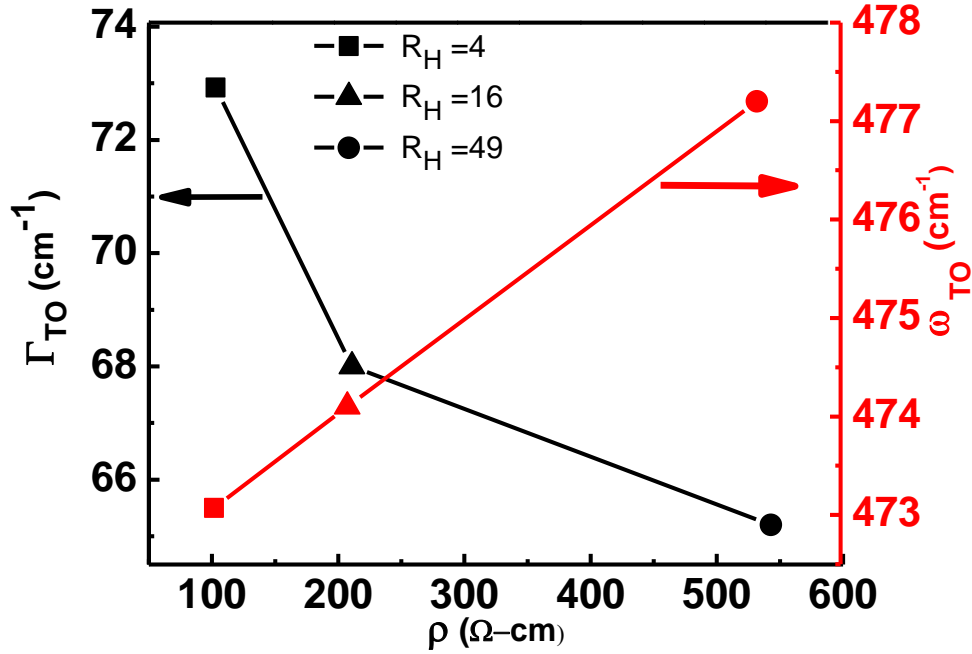


Figure 36. Line width and central frequency of TO mode vs. RT resistivity for “ r ” = 0.32, showing improvement in SRO and higher resistivity for higher H-dilution at 365 °C

Figure 36 shows a correlation of electrical resistivity with Γ_{TO} and ω_{TO} . In **Figure 36**, Γ_{TO} and ω_{TO} are plotted with respect to resistivity for various H-dilutions from 4 to 49 for samples with fixed boron doping ($r = 0.32$) and growth temperature (365 °C). The decrease in the linewidth and shift to higher wavenumber of the TO peak with increasing H-dilution indicate that there is a continuous improvement in the structure of the amorphous network on the short range scale. Thus, the increase in resistivity can be understood as a result of the improvement in the local order of the a-Si:H thin film. Similar results in fluorinated a-Si:H prepared by the glow discharge deposition method was reported by relating the central frequency of TO mode with the dark conductivity [60]. It will be interesting to determine if this applies to growth conditions other than H-dilution.

Correlation of Raman spectra with noise

In **Figure 37**, the noise parameter α_H/p is plotted with the TO linewidth of the Raman spectra for representative samples. From these limited data the normalized Hooke parameter seems to be improving (decreasing) with increasing TO linewidth, which depends on Hydrogen dilution, growth temperature and doping level.

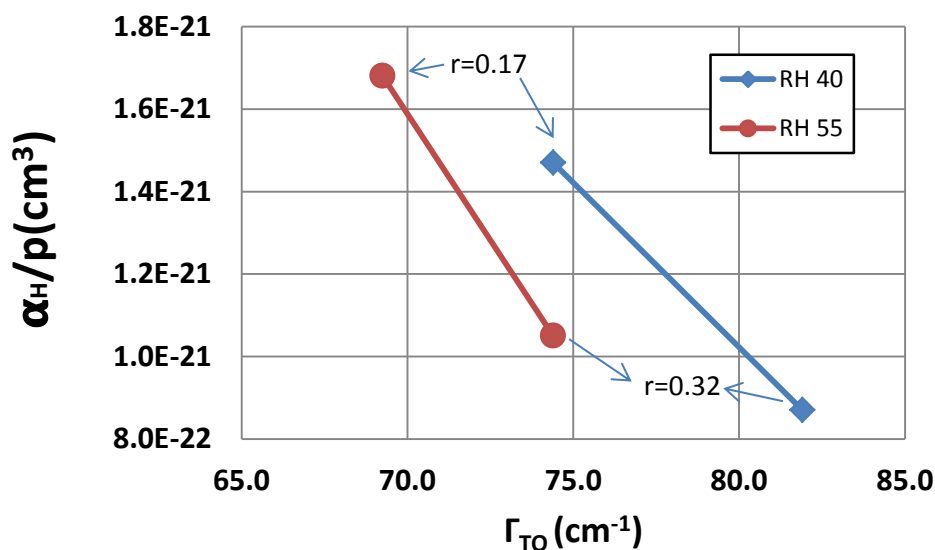


Figure 37. Correlation of normalized Hooke parameter α_H/p with Raman TO peak linewidth.

4.2 Multiple Internal Reflection Fourier Transform Infrared (MIR-FTIR) Spectroscopy

We employed Multiple Internal Reflection Fourier Transform Infrared Spectroscopy (MIR-IR) to characterize chemical bonding structure of boron doped hydrogenated amorphous silicon (*a*-Si:H). Samples of *a*-Si:H thin films were grown by PECVD on crystalline silicon wafers and on silicon wafers with a silicon nitride overlayer at 365 C substrate temperature.

Experimental

MIR-IR utilizes silicon wafer itself as an IR waveguide for attenuated total reflection (ATR) to achieve sub monolayer detection sensitivity [61]. Favorable difference of refractive indices of Si wafer and its air interface enables multiple total internal reflections (ca. 80 reflections from a 60 mm Si ATR crystal), which greatly enhances IR measuring sensitivity. The *a*-Si:H (ca. 50 nm) coated silicon wafers were fabricated on to an ATR optical element (60 x 10 x 0.7 mm, 45° bevel angle) by mechanical polishing [61]. For Si<100> background ATR coupons, Standard Cleaning (SC1) solution was used to remove any organic contamination from the surface followed by etching in 0.5% HF solution. IR spectra were recorded on a Nicolet IS 50 FTIR spectrometer

under constantly purged with dry air ($\text{CO}_2 < 1$ ppm). Both transmission (TIR) and MIR-IR infrared spectra were measured. All spectra were collected at 2 cm^{-1} resolution and are the average of 100 individual spectra. The detection limit of MIR-IR is ca. 0.2 mabs with an error margin of $< 3\%$.

Results

The infrared absorption spectra (MIR-IR and TIR) of an $a\text{-Si:H}$ thin film sample grown over $\text{Si}_x\text{N}_y\text{:H}$ coated $\text{Si}\langle 100 \rangle$ are shown in **Figure 38**. MIR-IR demonstrates over a hundred fold increase of detection sensitivity compared with conventional TIR. The multiple sampling enabled by more than 80 total internal reflections greatly enhances the measuring sensitivity of MIR-IR technique. Previously, we utilized MIR-IR to monitor hydrogen passivation on $\text{Si}\langle 100 \rangle$ surface with sub-monolayer measuring sensitivity [62]. The MIR-IR spectrum, **Figure 38**, reveals well-resolved IR absorption peaks associated with Si-H (1989 cm^{-1}) and B-H (2465 cm^{-1}) bonding modes originated from $a\text{-Si:H}$ thin film [63]. The observed infrared absorption peaks of N-H (3340 cm^{-1}) and SiH_x (2000 cm^{-1}) bonding modes can be assigned to the underlying $\text{Si}_x\text{N}_y\text{:H}$ layer on $\text{Si}\langle 100 \rangle$ substrate.

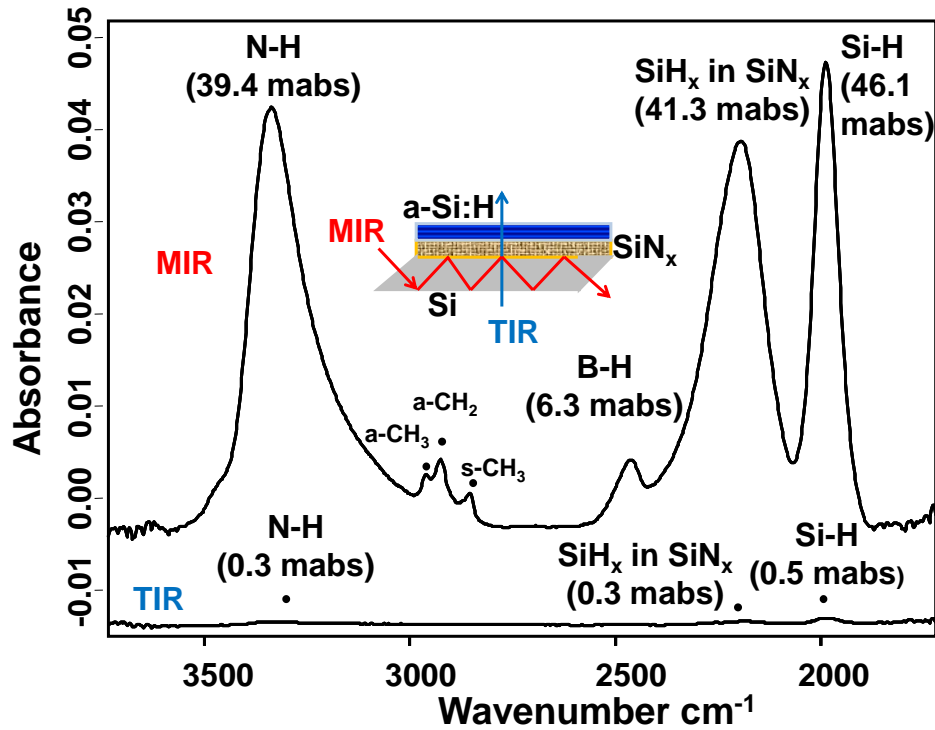


Figure 38. MIR-IR (top) and TIR (bottom) spectra of a 50 nm $a\text{-Si:H}$ thin film deposited on $\text{Si}_x\text{N}_y\text{:H}$

Effects of boron doping ratio and hydrogen dilution growth parameters on PECVD $a\text{-Si:H}$ thin film were studied by MIR-IR. **Figure 39 (a)** and **Figure 40 (a)** show that increasing of the boron doping ratio $r = [\text{BCl}_3]/[\text{SiH}_4]$ results in a continued, but a more pronounced decrease

of Si-H bonds. In **Figure 39 (b)** and **Figure 40 (b)**, when the hydrogen dilution ratio $R_H = [H_2]/[SiH_4]$ is increased in the boron doped a-Si:H deposition process, there is an increase in Si-H bond formation and a decrease in the B-H bond formation. Also, the N-H (3340 cm^{-1}) and Si-H_x (2000 cm^{-1}) infrared absorption peaks from underlying substrate Si_xN_y:H remain constant as expected in **Figure 39 (a)** and **Figure 39 (b)**.

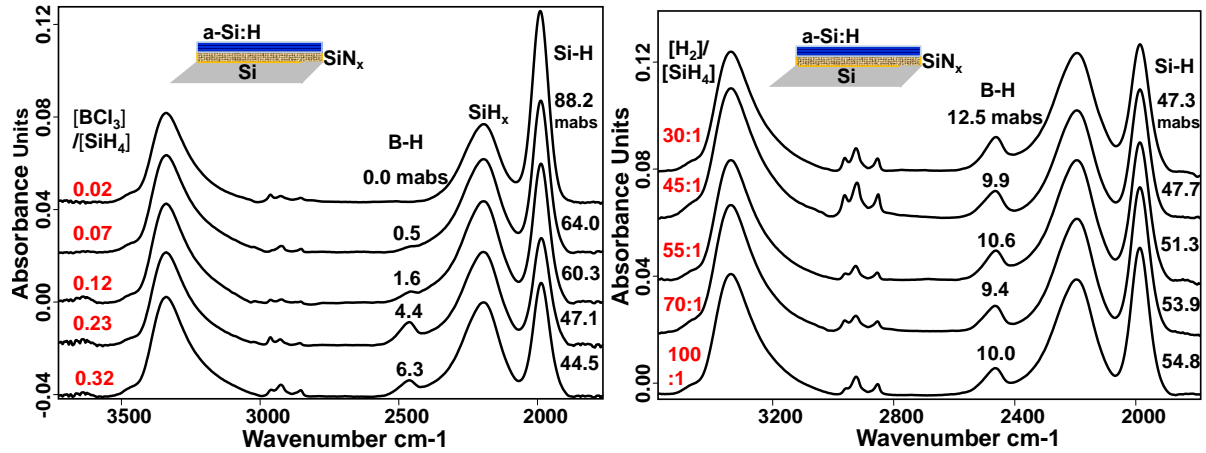


Figure 39. MIR-IR spectra of 50 nm a-Si:H thin films deposited on Si_xN_y:H with different PECVD grown parameters a) boron doping $[BCl_3]/[SiH_4]$ ratio, b) hydrogen dilution $[H_2]/[SiH_4]$ ratio

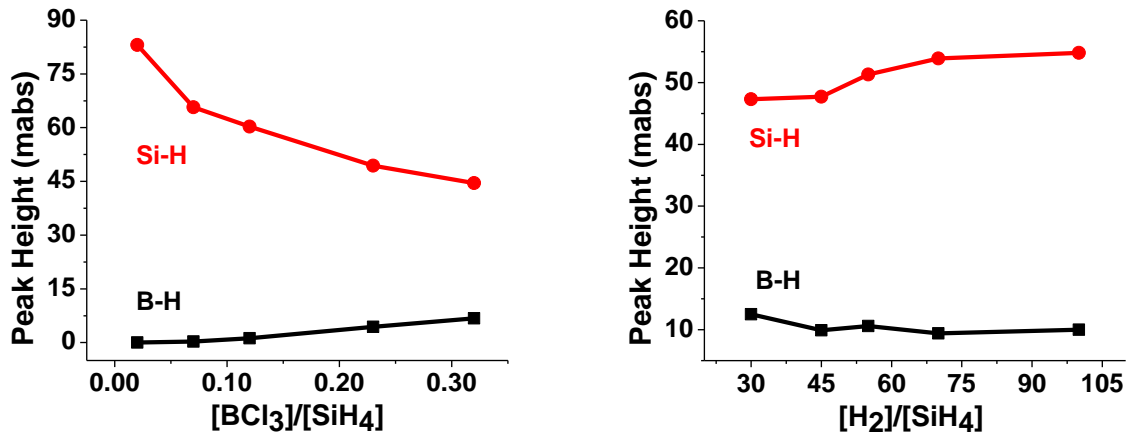


Figure 40. Effects of PECVD grown parameters a) boron doping $[BCl_3]/[SiH_4]$ ratio, b) hydrogen dilution $[H_2]/[SiH_4]$ ratio on IR absorption peaks heights of B-H and Si-H in a-Si:H thin films

As shown in **Figure 38**, the underlying Si_xN_y:H layer exhibits a strong SiH_x absorption peak centered at 2000 cm^{-1} that can mask the important chemical bonding information of PECVD a-Si:H film. To examine more closely the IR absorption at the region of $1800\text{--}2400\text{ cm}^{-1}$, a-Si:H thin films were deposited directly on Si<100> substrate. As **Figure 41** shows, by removing the Si_xN_y:H layer, two additional IR peaks at 2105 cm^{-1} and 2260 cm^{-1} were observed from a-Si:H thin film and can be assigned to SiH₂ and O-SiH_x bonding modes respectively [64]. Effects of

doping ratio and hydrogen dilution on *a*-Si:H thin film deposited on Si<100> substrate were also studied by MIR-IR. **Figure 42 (a)** and **Figure 42 (b)** confirm that an interesting counter-balance relationship exists between boron-doping and hydrogen-dilution growth parameters in PECVD-grown *a*-Si:H. Specifically, an increase in the hydrogen dilution ratio causes the increase in the Si-H bonding and a decrease in the B-H and Si-H₂ bonding. In comparison, an increase in B doping ratio results in the increase of B-H bonding and decrease of Si-H bonding mode.

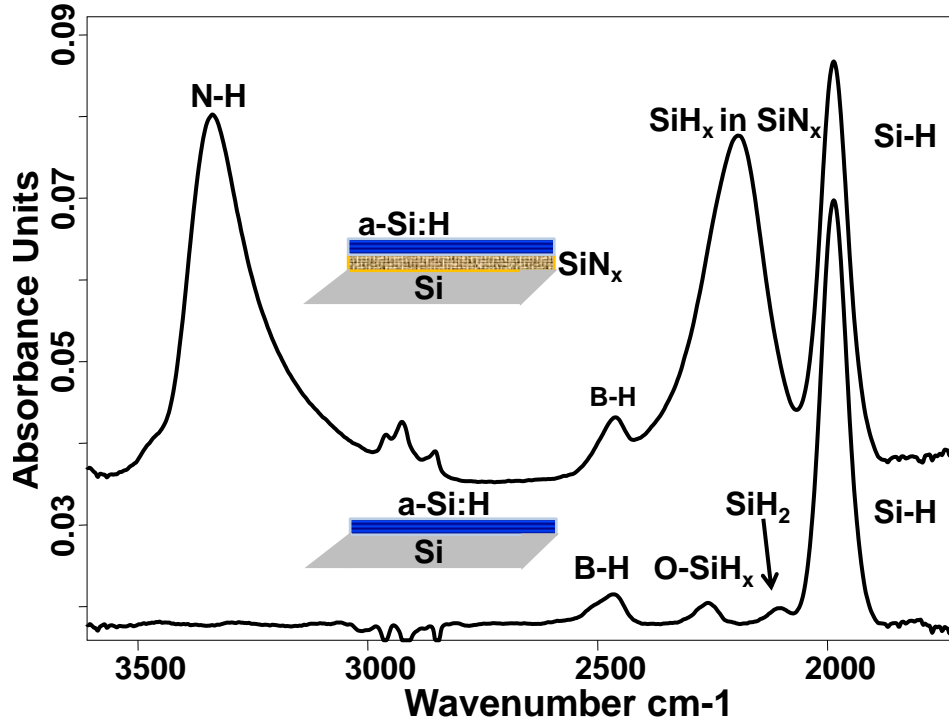


Figure 41. MIR-IR spectra of an *a*-Si:H thin film a) with a Si_xN_y:H underlying layer b) without a Si_xN_y:H underlying layer to reveal important SiH₂ and O-SiH_x peaks of *a*-Si:H .

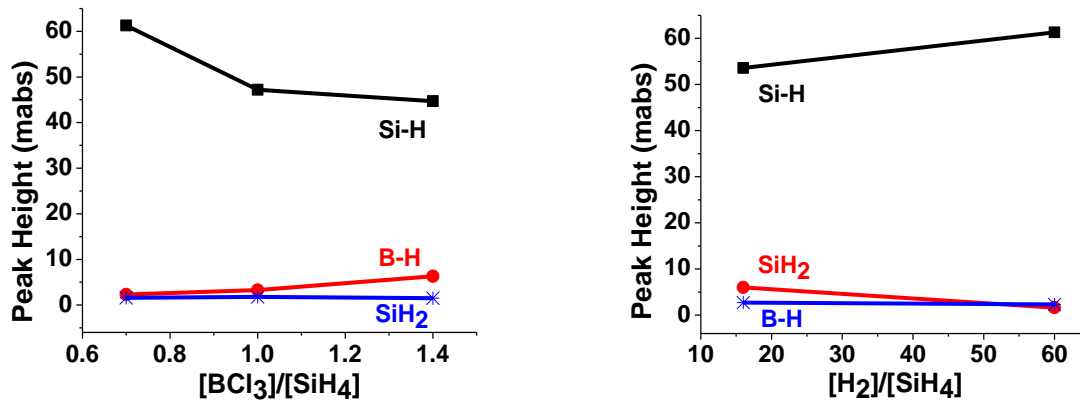


Figure 42. Effects of PECVD grown parameters: [BCl₃]/[SiH₄] ratio and [H₂]/[SiH₄] ratio on IR absorption peaks heights of B-H, SiH₂ and Si-H in *a*-Si:H thin films deposited on Si<100>

We have applied this technique to investigate the incorporation of hydrogen to better understand the role of hydrogen dilution in transitioning the a-Si:H from the amorphous to microcrystalline phase. This can be assessed by the determination of the microstructure ratio (R^*). In general, R^* is given by [65]:

$$R^* = [\text{Si-H}_2]/\{[\text{Si-H}_2] + \text{Si-H}\}, \quad \text{Eq. 57}$$

Here, the microstructure factor R^* is defined as the fraction of hydrogen with silane bonding among all hydrogen incorporated in the films. In practice, R^* can be determined by calculating the area bounded by the spectral resonances associated with Si-H ($\sim 2100 \text{ cm}^{-1}$) and Si-H₂ ($\sim 1990 \text{ cm}^{-1}$), seen in Figure 26, and taking the appropriate ratios.

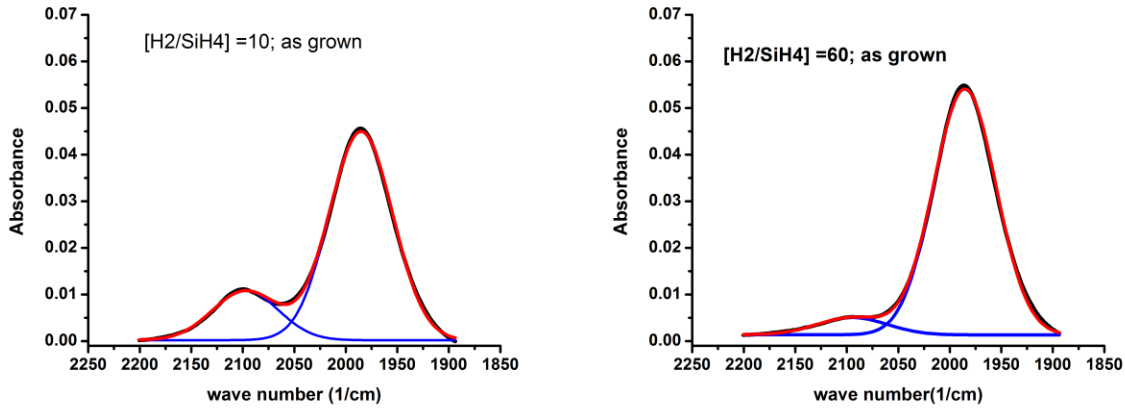


Figure 43. Absorbance MIR-FTIR spectra of Si-H and Si-H₂ for as-grown a-Si films of differing hydrogen dilution for a $[\text{BCl}_3]/[\text{SiH}_4]$ flow rate ratio of 0.32

Table 7 summarizes the results obtained from the analysis of spectra obtained for hydrogen dilution ratios $R_H = [\text{H}_2/\text{SiH}_4]$ of 10: 1 and 60:1.

Table 5. Microstructure factor analysis for hydrogen dilution ratios $[\text{H}_2/\text{SiH}_4]$ of 10:1 and 60:1

MIR-IR: As grown single layer a-Si:H thin film with $r = 0.32$						
	Area (a.u.)		Center frequency (cm^{-1})		FWHM (cm^{-1})	
	$[\text{H}_2/\text{SiH}_4]$ 10	$[\text{H}_2/\text{SiH}_4]$ 60	$[\text{H}_2/\text{SiH}_4]$ 10	$[\text{H}_2/\text{SiH}_4]$ 60	$[\text{H}_2/\text{SiH}_4]$ 10	$[\text{H}_2/\text{SiH}_4]$ 60
Si-H	3.441	4.011	1985.2	1985.5	72.2	71.4
Si-H ₂	0.852	0.316	2097.4	2094.7	75.6	79.8
$[\text{Si-H}_2] + \text{Si-H}$	4.293	4.327				
R^*	0.198	0.073				

From the area under the curve the microstructure factor (R^*) decreases from 0.198 to 0.073 as the hydrogen dilution R_H increases from 10 to 60, indicating a reduction of microvoids in the films, resulting in an improvement in both the short- and mid-range order. We note that improvement of the microstructure ratio R^* with H-dilution is also observed in *a*-Si:H films grown at lower substrate temperature (275 C). However R^* is about a factor of two higher for films grown at 275 C. The MIR analysis of R^* showing improvement in the structural organization of *a*-Si:H films with H-dilution is corroborated by Raman spectroscopic analysis. As shown in **Figure 34** the line width of the TO mode Γ_{TO} improves with H-dilution, indicating improvement in SRO with increase of H-dilution and the intensity ratio (I_{TA}/I_{TO}) decreases with H-dilution indicating improvement in MRO with increase of H-dilution.

Deposition Condition Effects on Chemical Bonding Structure

MIR-IR reveals four IR-active bonding modes including B-H, O-SiH_x, Si-H₂ and Si-H in the 50 nm *a*-Si:H thin film grown by PECVD. An interesting counter-balance relationship between boron-doping and hydrogen-dilution growth parameters was consistently observed in all *a*-Si:H films deposited on Si_xN_y:H or Si<100>. A simplistic explanation can be described as there is a competition between B and Si toward H during PECVD growth process. Based on bond energy calculations, B-H (389 KJ/mole) is more energetically favorable than Si-H (318 KJ/mole) [66]. Our MIR-IR data, **Figure 40 (a) vs. Figure 40 (b)**, show that an increase of boron-doping ratio gives a more pronounced decrease of Si-H bonds and steady increase of B-H bonds. However, PECVD growth process involves energetic ions, reactive radicals and neutral moieties from precursors that interacting with constant evolving surface with various active sites. More work is needed to give a reliable account of the observed counter-balance relationship. On the other hand, optimization of B-doping in *a*-Si:H films to achieve proper balance of temperature coefficient of resistance and conductivity is critical important for the infrared microbolometer imaging application. Our MIR-IR data bring new insights toward better understanding of detailed B-doping mechanism.

It is well known that B-doping in amorphous silicon is inefficient as compared to crystalline silicon [10]. The repeating crystal structure in *c*-Si favors B atoms to assume the fourfold configuration as its surrounding *c*-Si lattice. The resulting substitutional B doping provide mobile hole carriers to shift the Fermi-level and achieve active doping. However, relaxation effects in the amorphous matrix can significantly reduce the dominance of the fourfold substitutional doping. Several hypotheses have been proposed for explaining the cause of low doping efficiency of B in *a*-Si and *a*-Si:H. Most of B could be incorporated into threefold coordinate sites that are inert and non-doping [10]. In addition, localized midgap states commonly associated with dangling bonds as well as tail states in the valence and conduction bands could contribute to the non-active B doping configuration [10]. Recently, Santos et al. used *ab initio* simulations to propose the presence of intrinsic hole traps associated with highly distorted angles in the amorphous matrix [67]. Consequently, even the substitutional B doping in fourfold configuration can lose its hole carriers to these hole traps nearby. Hydrogen as the key compositional ingredient of *a*-Si:H and has been associated with the inactive B doping. Boyce and Ready [68] used NMR measurements to show one-half of all B atoms has a neighboring H atoms about 1.4 Å away and suggested H-passivation on B as the likely cause of non-active B doping. Fedders and Drabold proposed based on simulation that B(3,1) (a B with three Si and

one H neighbors) is the most favorable doping configuration energetically [69]. They also proposed that B-H pair formation, similar to *c*-Si, could disable the B-doping in *a*-Si:H by inserting a H atom between a B atom and one of its Si nearest neighbors.

Our MIR-IR analyses reveal detailed chemical bonding characteristics of B-doped *a*-Si:H thin film to collaborate with various theoretical predictions. As shown in **Figure 41**, B-doping generates mainly B-H bonding in the *a*-Si:H matrix observed as a vibrational mode at 2465 cm^{-1} . No higher H substitution on B, like BH_2 and BH_3 vibrational modes at $2500\text{--}2565\text{ cm}^{-1}$ [70], were observed. In addition, no three-centered-two-electron Si-H-B bridge formation was observed at 1850 cm^{-1} in the PECVD *a*-Si:H thin films up to B doping ratio of 0.32. Therefore, H-passivation via the B-H pair formation is not the main cause of inefficient B doping in our *a*-Si:H thin film. Previously, the resistivity *a*-Si:H thin film were shown to reach saturation after B doping ratio of 0.13 and further increase in B dopant concentration do not yield lower resistivity [28]. However, MIR-IR spectroscopic analyses show B-H bonding in *a*-Si:H continues to increase up to the tested B doping ratio of 0.32, **Figure 39 (a)**. The result suggests that the part of the inactive B-doping coordination configuration should include B-H bonding. We propose that the threefold coordination of B (2,1) (a B with two Si and one H neighbors) contributes to the inactive B-doping in PECVD grown *a*-Si:H thin films based on MIR-IR characterization.

5.0 Summary

The electrical conduction mechanisms and optical properties of boron doped hydrogenated amorphous silicon thin films (*a*-Si:H) were investigated to determine the effects of boron and hydrogen incorporation on carrier transport. Specifically, the temperature dependence of conductivity and temperature coefficient of resistance (TCR) were measured on boron doped *a*-Si:H films grown by plasma enhanced chemical vapor deposition (PECVD) at differing boron dopant source concentration and hydrogen dilution of the silane precursor. The key results are that the dominant conduction mechanism in p-type *a*-Si:H is by carrier hopping, the low frequency noise has a weak temperature dependence at lower temperatures, and film deposition at high temperature and/or at high H-dilution improve the atomic order in *a*-Si:H.

1. **Conductivity.** Carrier hopping is the dominant conduction mechanism in diverse groups of materials including disordered semiconductors, organic semiconductors, nanomaterials, and biomaterials. In p-type *a*-Si, Mott or Efros-Shklovskii Variable Range Hopping, is the dominant conduction mechanism depending on the temperature and the distribution of traps. It has been shown that for samples with moderate doping and hydrogen dilution, the electrical conductivity at temperatures between 100K and 425K is dominated by Mott Variable range hopping (M-VRH). This conclusion is further supported by resistance curve derivation analysis (RCDA) of the electrical conductivity, confirming the temperature dependence predicted by the Mott conduction mechanism. However, for highly doped, lower dilution samples at lower temperatures ($T < 100\text{K}$), the conductivity deviates from that predicted by M-VRH and is described by Efros – Shklovskii variable range hopping conduction (ES-VRH), where the long

range coulomb interaction between carriers, neglected by Mott, reduces the density of states to zero in the vicinity of the Fermi level, creating a so-called 'Coulomb gap'.

2. **Noise.** The noise at temperatures lower than $\sim 400\text{K}$ is dominated by a $1/f$ component which follows the Hooge model and correlates with the Mott conductivity. At high temperatures there is an appreciable G-R noise component.

3. **Atomic Structure.** High temperature deposition and/or high H-dilution improve the atomic order (lower defect density) as determined by Raman and MIR spectroscopies. The line width and frequency of the Raman TO Raman peak correlate with electrical measurements and can be used for non-destructive characterization of a-Si:H.

4. **Boron-Hydrogen bonding.** MIR-IR spectroscopy shows well-resolved bonding modes of B-H, SiH_2 and Si-H. B-H bonds can form electrically active fourfold coordinated bonding. The doping efficiency is influenced by an observed counter dependence of B-H and Si-H chemical bonds on boron dopant supply and on hydrogen dilution of silane.

6.0 Bibliography

1. P. A. Bell , C. W. Hoover, S. J. Pruchnic, “Standard NETD test procedure for FLIR systems with video output” SPIE Proc. Vol. 1969, p. 194 (1993)
2. R. A. Street (ed.), *Technology and Applications of Amorphous Silicon*, Springer, 2000.
3. J. Brady, T. Schimert, D. Ratcliff, R. Gooch, B. Ritchey, W. L. McCardel, K. Rachels, S. Ropson, M. Wand, M. Weinstein, and J. Wynn, *Proc. SPIE* Vol. **3698**, 161 (1999).
4. J. L. Tissot, F. Rothan, C. Vedel, M. Vilain, and J. J. Yon, *Proc. SPIE* Vol. **3436**, 605 (1998).
5. K. Tanaka, E. Maruyama, T. Shimada, and H. Okamoto, *Amorphous Silicon*, John Wiley & Sons, 1993.
6. R.W. Collins, A.S. Ferlauto, G.M. Ferreira, J. Koh, C. Chen, R.J. Koval, J.M. Pearce, C.R. Wronski, M.M. Al-Jassim, and K.M. Jones, “Application of deposition phase diagrams for the optimization of a-Si:H based materials and solar cells”, *Mat. Res. Soc. Symp. Proc.* Vol. **762**, A10.1.1 (2003).
7. W. E. Spear and P. G. Le Comber, *Solid State Commun.*, 17, 671(1975)
8. N.F. Mott and E.A. Davis, “Electronic processes in non-crystalline materials,” Clarendon Press, Oxford, 1979.
9. A. L. Efros and B. I. Shklovskii, “ Electronic Properties of Doped Semiconductors,” Springer-Verlag, Berlin, 1984.
10. R.A. Street, “Hydrogenated amorphous silicon”, Cambridge University Press
11. Ralph Rosenbaum “Crossover from Mott to Efros-Shklovskii variable-range-hopping conductivity in In_xO_y films”, *Phy. Rev. B*, Vol. 44, Num. 8, (1991).
12. R. Abdia, A. El Kaaouachi , A. Nafidi, G. Biskupski , J. Hemine “ Variable range hopping conductivity and negative magnetoresistance in n-type InP semiconductor”, *Solid state electronics* 53, (2009).
13. Thejal Abraham, Chandrahas Bansal, J. Thampi Thanka Kumaran, and Ashok Chatterjee, “Efros-Shklovskii variable range hopping transport in nanocluster metallic films,” *J. Appl. Phys.* 111, 104318 (2012).
14. N. Aoki, K. Nara, and Y. Ochiai “Coulomb Gap Energy in Amorphous SixGe_{1-x} Films”, *phys. stat. sol. (b)* 218, 5 (2000) Moon Sung Kang, Ayaskanta Sahu, David J. Norris, and C. Daniel Frisbie, *Nano Lett.* 11, 3887 (2011).
15. This program
16. Abdullah Yildiz, Necmi Serin, Tulay Serin, and Mehmet Kasap “Crossover from Nearest-Neighbor Hopping Conduction to Efros–Shklovskii Variable-Range Hopping

Conduction in Hydrogenated Amorphous Silicon Films”, Japanese Journal of Applied Physics, Vol. 48 (2009).

17. S. S. N. Bharadwaja, C. Venkatasubramanian, N. Fieldhouse, S. Ashok, M. W. Horn and T. N. Jackson, “Low temperature charge carrier hopping transport mechanism in vanadium oxide thin films grown using pulsed dc sputtering.” Appl. Phys. Lett 94 222110 (2009).
18. A. Yildiz, S.B. Lisesivdin, M. Kasap, D. Mardare, “Electrical properties of TiO₂ thin films, :” JNCS 354, 4944 (2008).
19. Ralph Rosenbaum “Crossover from Mott to Efros-Shklovskii variable-range-hopping conductivity in In_xO_y films”, Phy. Rev. B, Vol. 44, Num. 8, (1991).
20. Jun Wang, Xiaoshuang Chen, Weida Hu, Lin Wang, Wei Lu, Faqiang Xu, Jun Zhao, Yanli Shi and Rongbin J, “Amorphous HgCdTe infrared photoconductive detector with high detectivity above 200 K,” APL 99, 113508 (2011).
21. Moon Sung Kang, Ayaskanta Sahu, David J. Norris, and C. Daniel Frisbie, “Size- and Temperature-Dependent Charge Transport in PbSe Nanocrystal Thin Films,” Nano Lett. 2011, 11, 3887-3892.
22. Heng Liu , Alexandre Pourret, and Philippe Guyot-Sionnest, “Mott and Efros-Shklovskii Variable Range Hopping in CdSe Quantum Dots Films,” ACS Nano, 4, No 9, 5211-5216, 2010.
23. Chiashain Chuanga, R.K. Puddy, Huang-De Lin, Shun-Tsung Lo, T.-M. Chen, C.G. Smith, C.-T. Liang, “Experimental evidence for Efros–Shklovskii variable range hopping in hydrogenated graphene,” Solid State Comm. 152 (2012) 905–908.
24. Z.H. Khan, S. Husain, M. Husain, “Variable range hopping in carbon nanotubes,” Current Nanoscience, 2010, 6, 626-641.
25. Aleshin, A. N., Sandberg, H., Stubbs, H., “Two-dimensional charge carrier mobility studies of regioregular P3HT,” Synthetic Metals 121 (2001) 1449.
26. Z. G. Yu and Xueyu Song, “Variable Range Hopping and Electrical Conductivity along the DNA Double Helix,” Phys. Lett., 86, 6018 (2001).
27. Hans-Werner Fink & Christian Schoenenberger, “Electrical conduction through DNA molecules,” Nature (London) 398, 407 (1999).

28. S. K. Ajmera, A.J. Syllaos, Gregory S. Tyber, Michael F. Taylor, and Russell E. Hollingsworth, "Amorphous silicon thin-films for uncooled infrared microbolometer sensors," Proc. of SPIE 7660, 12-1 - 12-8 (2010).
29. B. I. Shklovskii, "1/f noise in variable range hopping conduction", Phys. Rev., B 67, 045201 (2003)
30. A. L. Burin, B. I. Shklovskii, V. I. Kozub, Y. M. Galperin, and V. Vinokur, "Many electron theory of 1/ f noise in hopping conductivity", Phys. Rev., B 74, 075205 (2006)
31. B. von Roedern, L. Ley, and M. Cardona "Photoelectron Spectra of Hydrogenated Amorphous Silicon", Vol. 9, Num. 24, Phy. Rev.Lett. 12, Dec (1977)
32. P.J. Zanzucchi, C.R. Wronski, and D.E. Carlson "Optical and photoconductive properties of discharge produced amorphous silicon", Journal of Applied Physics 48, 5227 (2008).
33. Sunhwa Lee, Seungman Park, Jinjoo Park, Youngkuk Kim, Kichan Yoon, Chonghoon Shin, Seungsin Baek, Joondong Kim, Youn-Jung Lee, and Junsin Yi "The Effect of Carrier Injection Stress on Boron-Doped Amorphous Silicon Suboxide Layers Investigated by X-ray Photoelectron Spectroscopy", J. Journal of App. Phy. 50 (2011) 095801; DOI: 10.1143/JJAP.50.095801.
34. A.G. Zabrodskii ,” The Coulomb gap: The view of an Experimenter”, philosophical Magazine part B, 81:9,1131-1151].
35. Anshuman Dalvi, N. Parvathala Reddy, S.C. Agarwal "The Meyer–Neldel rule and hopping conduction", Solid State Communications 152 (2012) 612–615, doi:10.1016/j.ssc.2012.01.018.
36. Zishan H. Khan "Electrical and optical properties of thin film of amorphous silicon nanoparticles", Applied Surface Science 255 (2009) 8874–8878
37. A. Yildiz and M. Kasap"Variable-Range Hopping Conductivity in InGaN", CP899, Sixth International Conference of the Balkan Physical Union, edited by S. A. Cetin and I. Hikmet© 2007 American Institute of Physics.
38. H. Overhof "The Mott Memorial Lecture: Fundamental concepts in the physics of amorphous Semiconductors", J. of Non-Crystalline Solids 227–230 (1998) 15–22.
39. F. N. Hooge, IEEE Trans Elect Dev 41, 1926 (1994)
40. S. Mouetsi, A. El Hdiy, and M. Bouchemat, M. J. Cond. Matter 12, (No 3) 204 (2010)

41. A. K. Rice and K. J. Malloy, J. Appl. Phys. 87 (No 11), 7892 (2000)
42. Jeffrey S. Lannin, "Structural order and dynamics of amorphous Si and Ge", J. of Non-Cryst. Solids, 97 & 98 (1987) 203-206.
43. J. Forner and J.S. Lannin, "Short range order variations in amorphous silicon", J. of Non-Cryst. Solids, 106 (1988) 128-131.
44. J. Forner and J.S. Lannin, "Radial distribution functions of amorphous silicon" Phys. Rev. B, 39 (1989) 5527-5532.
45. R. Alben, E. Weair, J.E. Smith, Jr., and M.H. Brodsky, "Vibrational properties of amorphous Si and Ge", Phys. Rev. B 11 (1975) 2271.
46. S. Gupta, R.S. Katiyar, S.Z. Weisz, I. Balberg, "The effect of light soaking on the structural order in a-Si:H" J. Non-Cryst. Solids, 266-269 (2000) 496-500.
47. J.S. Lannin, L.J. Pilione, S.T. Kshirsagar, R. Messier and R.C. Ross, "Variable structural order in amorphous silicon", Phys. Rev.B 26 (1982) 3506-3509
48. Maley, N. and Lannin, J. S., "Influence of hydrogen on vibrational and optical properties of a-Si_{1-x}H_xalloys", Phys. Rev.B 36 (1987) 1146-1152.
49. C.R. Wronski and R.W. Collins, "Phase engineering of a-Si:H solar cells for optimized performance", Solar Energy, 77 (2004) 877-885.
50. R. Saleh and N.H. Nickel, "Raman spectroscopy of B-doped microcrystalline silicon films", Thin Solid Films, 427 (2003) 266-269.
51. H. Chen, M.H. Gullanara, W.Z. Shen, "Effects of high hydrogen dilution on the optical and electrical properties in B-doped nc-Si:H thin films", J. of Crystal Growth, 260 (2004) 91-101.
52. Saravanapriyan Sriraman, Sumit Agarwal, Eray S. Aydil and Dimitrios Maroudas, "Mechanism of hydrogen-induced crystallization of amorphous silicon", Nature, 418 (2002) 62-65.
53. N. Ross, K. Shrestha, O. Chyan, C. L. Littler, V. C. Lopes, and A. J. Syllaios, "Spectroscopic Study of the Chemical Bonding Structure in Amorphous Silicon Thin Films", MRS Proceedings, Vol. 1536/2013, DOI: <http://dx.doi.org/10.1557/opl.2013.752>.

54. Saravanapriyan Sriraman, Sumit Agarwal, Eray S. Aydil and Dimitrios Maroudas, "Mechanism of hydrogen-induced crystallization of amorphous silicon", *Nature*, 418 (2002) 62-65.
55. S. C. Chen and M. Cardona; "Infrared and far-infrared absorption of B- and P-doped amorphous Si", *Phys. Rev. B*, Vol. 23, May (1981)
56. A. J. Syllaos, S. K. Ajmera, G. S. Tyber, C. Littler, R. E. Hollingsworth "Raman Characterization of Protocrystalline Silicon Films", *Mater. Res. Soc. Symp. Proc.* Vol. 1153, 2009.
57. P Danesh, B Pantchev, K Antonova, E Liarokapis, B Schmid, D Grambole and J Baran, "Hydrogen bonding and structural order in hydrogenated amorphous silicon prepared with hydrogen-diluted silane", *J. Phys. D: Appl. Phys.*, Vol. 37, (2004).
58. S. Chakraborty and D. Drabold, *Phys. Rev. B* 79 (2009) 115214.
59. Hishikawa, "Raman study on the variation of the silicon network of a-Si:H", *J. Appl. Phys.*, 62, (1987) 3150-3155.
60. R. Tsu, J. Gonzalez-Hernandez, J. Doehler and S.R. Ovshinsky, "Order Parameters in a-Si Systems", *Solid State Communications*, 46 (1983) 79-82.
61. D. Bhattacharyya, K. Pillai, O. Chyan, L. Tang, R.B. Timmons, *Chem. Mater.* 19, 2222 (2007)
62. O. Chyan, J. Wu, J.J. Chen. *Appl. Spec.* 51, 1905 (1997)
63. C. Guanghua, Z. Chenzhi, Z. Angqing, C. Jinlong and C. Wei. *Phys. Stat. Sol.* 96, K187 (1986)
64. C. Liu, S. Palsule, Yi, S. Gangopadhyay. *Phys. Rev. B* 49, (1994)
65. O.S. Panwar, C. Mukherjee, R. Bhattacharyya, "Effect of annealing on the electrical, optical and structural properties of hydrogenated amorphous silicon films deposited in an asymmetric R.F. plasma CVD system at room temperature," *Solar Energy Material and Solar Cells* 57, 373 (1999)
66. T.L. Cottrell, *The Strengths of Chemical Bonds*, 2nd ed. (Butterworths Scientific Publication, London, 1958)
67. Santos, P. Castrillo, W. Windl, D.A. Drabold, L. Pelaz and L.A. Marques, *Phys. Rev. B* 81, (2010)
68. J. B. Boyce and S. E. Ready, *Phys. Rev. B* 38, 11008 (1998)
69. P.A. Fedders and D.A. Drabold, *Phys. Rev. B* 54, 1864 (1997)
70. G. Socrates. *Infrared and Raman Characteristic Group Frequencies*. (John Wiley & Sons, USA, 2001, 247-253)

Report Title

Final Report: Analysis of Electrical Transport and Noise Mechanisms in Amorphous Silicon

ABSTRACT

The objective of this program is to investigate the mechanisms of electrical conduction in amorphous silicon and identify factors affecting the performance of uncooled imaging focal plane array systems based on amorphous silicon microbolometer thermal detector structures. Measurements of the temperature dependence of conductivity and noise show that the dominant conduction mechanism in p-type a-Si:H is that of Mott variable range hopping. The hopping parameters are controlled by the film deposition conditions such as hydrogen dilution of the silane precursor and boron dopant level. The low frequency noise has a weak temperature dependence and is dominated by a $1/f$ component which follows the Hooge model and is correlated to the conductivity hopping parameters and in turn to the temperature coefficient of resistance (TCR). At high temperatures there is a generation-recombination (G-R) noise component. Raman spectroscopy measurements show that, with an increase of hydrogen dilution and/or growth temperature, both short and mid-range order improve, whereas the addition of boron results in the degradation of short range order. Multiple Internal Reflection IR spectroscopy of boron – hydrogen bonding in amorphous silicon shows B-H bonding configurations only. The B-H bonds can form electrically active fourfold coordinated bonding with silicon.

Enter List of papers submitted or published that acknowledge ARO support from the start of the project to the date of this printing. List the papers, including journal references, in the following categories:

(a) Papers published in peer-reviewed journals (N/A for none)

<u>Received</u>	<u>Paper</u>
01/05/2015	4.00 K. Shrestha, D. Whitfield, V. C. Lopes, A. J. Syllaos, C.L. Littler. Electrical Conductivity and Structural Order of p-Type Amorphous Silicon Thin Films, MRS Proceedings, (01 2015): 0. doi: 10.1557/opl.2014.962
06/02/2015	5.00 V.C. Lopes, A.J. Syllaos, D. Whitfield, K. Shrestha, C.L. Littler. $1/f$ Noise in Mott Variable Range Hopping Conduction in p-type Amorphous Silicon, MRS Proceedings, (06 2015): 0. doi: 10.1557/opl.2015.546
07/02/2013	1.00 A. J. Syllaos, V. C. Lopes, E. Hanson, D. Whitfield, K. Shrestha, C. L. Littler. Temperature Dependence of $1/f$ Noise and Electrical Conductivity Measurements on p-type a-Si:H Devices, MRS Proceedings, (06 2013): 0. doi: 10.1557/opl.2013.751
07/02/2013	2.00 N. Ross, K. Shrestha, O. Chyan, C. L Littler, V. C. Lopes, A. J. Syllaos. Characterization of Boron Doped Amorphous Silicon Films by Multiple Internal Reflection Infrared Spectroscopy, MRS Proceedings, (06 2013): 0. doi: 10.1557/opl.2013.752
09/24/2014	3.00 K. Shrestha, V.C. Lopes, A.J. Syllaos, C.L. Littler. Raman spectroscopic investigation of boron doped hydrogenated amorphous silicon thin films, Journal of Non-Crystalline Solids, (11 2014): 80. doi: 10.1016/j.jnoncrysol.2014.07.013
TOTAL:	5

Number of Papers published in peer-reviewed journals:

(b) Papers published in non-peer-reviewed journals (N/A for none)

Received Paper

TOTAL:

Number of Papers published in non peer-reviewed journals:

(c) Presentations

1.A. J. Syllaios, V. C. Lopes, C. L. Littler, S.K. Ajmera, M. Chitteboyina "Low frequency noise in p-type amorphous silicon thin films" presented at the 2015 Military Sensing Symposia (MSS) Parallel Meeting.

Number of Presentations: 1.00

Non Peer-Reviewed Conference Proceeding publications (other than abstracts):

Received Paper

TOTAL:

Number of Non Peer-Reviewed Conference Proceeding publications (other than abstracts):

Peer-Reviewed Conference Proceeding publications (other than abstracts):

Received Paper

TOTAL:

Number of Peer-Reviewed Conference Proceeding publications (other than abstracts):

(d) Manuscripts

Received Paper

TOTAL:

Number of Manuscripts:

Books

Received Book

TOTAL:

Received Book Chapter

TOTAL:

Patents Submitted

Patents Awarded

Awards

Graduate Students

NAME

PERCENT SUPPORTED

FTE Equivalent:

Total Number:

Names of Post Doctorates

NAME

PERCENT SUPPORTED

FTE Equivalent:

Total Number:

Names of Faculty Supported

NAME

PERCENT SUPPORTED

National Academy Member

Christopher L. Littler

0.12

FTE Equivalent:

0.12

Total Number:

1

Names of Under Graduate students supported

NAME

PERCENT SUPPORTED

FTE Equivalent:

Total Number:

Student Metrics

This section only applies to graduating undergraduates supported by this agreement in this reporting period

The number of undergraduates funded by this agreement who graduated during this period: 0.00

The number of undergraduates funded by this agreement who graduated during this period with a degree in science, mathematics, engineering, or technology fields:..... 0.00

The number of undergraduates funded by your agreement who graduated during this period and will continue to pursue a graduate or Ph.D. degree in science, mathematics, engineering, or technology fields:..... 0.00

Number of graduating undergraduates who achieved a 3.5 GPA to 4.0 (4.0 max scale):..... 0.00

Number of graduating undergraduates funded by a DoD funded Center of Excellence grant for Education, Research and Engineering:..... 0.00

The number of undergraduates funded by your agreement who graduated during this period and intend to work for the Department of Defense 0.00

The number of undergraduates funded by your agreement who graduated during this period and will receive scholarships or fellowships for further studies in science, mathematics, engineering or technology fields: 0.00

Names of Personnel receiving masters degrees

NAME

Total Number:

Names of personnel receiving PhDs

<u>NAME</u>

Total Number:

Names of other research staff

<u>NAME</u>	<u>PERCENT SUPPORTED</u>
-------------	--------------------------

Vincent C. Lopes	0.10
------------------	------

FTE Equivalent:	0.10
------------------------	-------------

Total Number:	1
----------------------	----------

Sub Contractors (DD882)

Inventions (DD882)

Scientific Progress

See attachment

Technology Transfer

Interaction with Industry. The findings of this program have been transferred to L-3 Communications Infrared Products, a manufacturer of uncooled infrared sensors.